

# Chapter 9

## Wide-Field ODMR and Camera Integration

*Parallel Quantum Readout for High-Throughput Field Imaging*

This chapter develops the **parallel detection component** of the measurement operator  $\mathcal{M}$ , establishing how camera-based ODMR enables  $N_{\text{parallel}} \gg 1$  that dominates the throughput term in  $Q_{\text{FOM}}$ .

**Operator Focus:**

- **Measurement operator  $\mathcal{M}$ :** Wide-field ODMR as parallel quantum readout converting NV fluorescence to spatially-resolved field maps
- **Data operator  $\mathcal{D}$ :** Camera noise model (photon shot noise, read noise, PRNU, speckle) determining measurement uncertainty
- **Calibration:** Flat-field correction and speckle reduction to maintain  $\Gamma_{\text{mm}} > 0.95$

**Key Achievements:**

- Rigorous ODMR signal model derived from Bloch equations including alternative lineshapes
- Complete camera noise model with analytical derivations for all noise sources
- Effective parallelism concept:  $N_{\text{eff}}$  accounting for sensitivity non-uniformity
- Information-theoretic foundation for compressed sensing ODMR speedup
- Three worked examples covering system design, calibration, and optimization

Wide-field ODMR is **Quantum Field Metrology (QFM)**—it produces calibrated field maps  $F(\mathbf{r})$ . The transition to **Quantum Field Imaging (QFI)** requires coupling with the reconstruction operator  $\mathcal{R}$  (Chapters 14–15). This chapter establishes the measurement quality metrics ( $\Gamma_{\text{mm}}$ , effective  $N_{\text{parallel}}$ ) that propagate to reconstruction fidelity  $\Gamma_{\text{inv}}$ .

**QFI Pipeline Position:**  $S(\mathbf{r}) \xrightarrow{\mathcal{G}} F(\mathbf{r}) \xrightarrow{\mathcal{M} \text{ (this chapter)}} D \xrightarrow{\mathcal{R}} \hat{S}(\mathbf{r}) \pm \sigma_S$

## Abbreviated Terms

Abbrev.	Definition	Abbrev.	Definition
ADC	Analog-to-Digital Converter	MW	Microwave
CCD	Charge-Coupled Device	NV	Nitrogen-Vacancy
CMOS	Complementary Metal-Oxide-Semiconductor	ODMR	Optically Detected Magnetic Resonance
CS	Compressed Sensing	PRNU	Photo-Response Non-Uniformity
EMCCD	Electron-Multiplying CCD	PSF	Point Spread Function
FOV	Field of View	QE	Quantum Efficiency
FPN	Fixed Pattern Noise	QFI	Quantum Field Imaging
FWHM	Full Width at Half Maximum	QFM	Quantum Field Metrology
ISC	Intersystem Crossing	RIP	Restricted Isometry Property
ML	Machine Learning	ROI	Region of Interest
MTF	Modulation Transfer Function	sCMOS	Scientific CMOS
		SNR	Signal-to-Noise Ratio
		ZFS	Zero-Field Splitting

Table 9.1: Abbreviated terms used in Chapter 9.

## Abstract

Wide-field optically detected magnetic resonance (ODMR) represents the critical technology that enables the parallelism factor  $N_{\text{parallel}} \gg 1$  in the QFI Figure of Merit. This chapter develops the complete theory and practice of camera-based ODMR detection, establishing the bridge between single-NV physics (Chapters 7–8) and system-level forward models (Part IV). We derive the ODMR signal model from first principles using Bloch equations, extending beyond the standard Gaussian lineshape to address Lorentzian, Voigt, and structured spectra arising from non-ideal ensembles. The complete camera noise model is developed with full analytical derivations for photon shot noise, read noise, dark current, photo-response non-uniformity (PRNU), and speckle noise from coherent illumination, showing how each noise source propagates to the reconstruction fidelity factor  $\Gamma_{\text{mm}}$ . We introduce the concept of *effective parallelism*  $N_{\text{eff}}$  that accounts for sensitivity non-uniformity across the field of view, providing realistic throughput estimates. Lock-in detection techniques for wide-field ODMR are presented with detailed signal processing analysis. A rigorous information-theoretic treatment of compressed sensing ODMR establishes the fundamental speedup limits based on spectral sparsity and the Restricted Isometry Property. Three comprehensive worked examples guide system design, PRNU calibration, and lock-in parameter optimization.

## 9.1 Introduction: Why Wide-Field ODMR Matters

### 9.1.1 The Throughput Imperative

The QFI Figure of Merit established in Chapter 1 explicitly contains the parallelism factor:

#### QFI Figure of Merit

$$Q_{\text{FOM}} = \frac{\eta_q}{\eta_{\text{classical}}} \times \frac{N_{\text{parallel}}}{t_{\text{acquisition}}} \times \Phi_{\text{multi}} \quad (9.1)$$

The term  $N_{\text{parallel}}/t_{\text{acquisition}}$  represents the measurement throughput—the number of independent measurement channels acquired per unit time. For a scanning confocal system measuring point-by-point,  $N_{\text{parallel}} = 1$ , and mapping a field requires  $N_{\text{pixels}}$  sequential acquisitions. In contrast, a camera-based wide-field system achieves  $N_{\text{parallel}} = 10^4$  to  $10^6$  pixels simultaneously.

### Derivation: Throughput Advantage Quantification

Consider mapping a  $100 \times 100 \mu\text{m}$  area with  $1 \mu\text{m}$  resolution, requiring  $N_{\text{pixels}} = 10,000$  measurement points.

#### Scanning confocal approach:

- Dwell time per pixel:  $t_{\text{dwell}} = 10 \text{ ms}$  (typical for  $\mu\text{T}$  sensitivity)
- Stage settling time:  $t_{\text{settle}} = 5 \text{ ms}$
- Total time:  $T_{\text{scan}} = N_{\text{pixels}} \times (t_{\text{dwell}} + t_{\text{settle}}) = 10,000 \times 15 \text{ ms} = 150 \text{ s}$

#### Wide-field camera approach:

- Camera integration:  $t_{\text{int}} = 10 \text{ ms}$  (same photon budget per pixel)
- All pixels acquired simultaneously
- Total time:  $T_{\text{wide}} = t_{\text{int}} = 10 \text{ ms}$

#### Throughput advantage:

$$\frac{T_{\text{scan}}}{T_{\text{wide}}} = \frac{150 \text{ s}}{0.01 \text{ s}} = 15,000 \times \quad (9.2)$$

This factor of  $> 10^4$  throughput improvement is the fundamental motivation for wide-field ODMR in QFI applications.

For semiconductor failure analysis where a 300 mm wafer contains  $> 10^9$  potential defect sites, only wide-field approaches can achieve economically viable inspection throughput.

### 9.1.2 Historical Development

The evolution of wide-field ODMR reflects the interplay between detector technology and NV center understanding:

Table 9.2: Historical milestones in wide-field NV imaging.

Year	Milestone	Significance
2008	First wide-field NV imaging	Epstein et al. demonstrated CCD-based detection
2011	Current imaging in IC	Nowodzinski et al. showed FA application
2015	High-resolution B-field mapping	Glenn et al. achieved $\mu\text{m}$ -scale resolution
2017	Lock-in wide-field ODMR	Horsley et al. improved SNR by $10\times$
2019	Video-rate magnetic imaging	Real-time dynamic current mapping
2021	Commercial QFM systems	First turnkey wide-field magnetometers
2023	Integration with FA workflow	QFI demonstrated for 3D IC inspection

### 9.1.3 Pain Points in Wide-Field ODMR

Despite the throughput advantage, wide-field ODMR introduces challenges that this chapter addresses:

1. **PRNU (Photo-Response Non-Uniformity):** Pixel-to-pixel sensitivity variations ( $\sim 1\text{--}3\%$ ) create systematic field errors. Without correction, PRNU creates a fundamental SNR ceiling:  $\text{SNR}_{\max} = 1/\text{PRNU}$ . For 1.5% PRNU, this limits SNR to 67 regardless of photon flux. Section 9.4 develops calibration protocols.
2. **Read noise floor:** Unlike photomultipliers or avalanche photodiodes, camera pixels have additive read noise ( $\sigma_{\text{read}} \sim 1\text{--}10 e^-$ ) that limits low-light performance. Section 9.3.3 analyzes operating regimes.
3. **ODMR contrast reduction:** Single NV centers exhibit 30% ODMR contrast, but ensembles show only 1–10% due to:
  - Orientation averaging: Only 1/4 of NV centers align with any given field direction
  - Strain inhomogeneity: Distributed  $E$  parameter broadens and reduces resonance
  - Power broadening: High optical/MW power needed for wide-field reduces contrast

Section 9.2.7 derives contrast dependencies.

4. **FOV-sensitivity trade-off:** Expanding the FOV beyond the uniformly-illuminated region captures more pixels but with degraded sensitivity. Section 9.7.4 introduces effective parallelism  $N_{\text{eff}}$ .
5. **Speckle noise:** Coherent laser illumination creates intensity variations that add measurement uncertainty. Section 9.3.4 analyzes speckle statistics and reduction techniques.

### 9.1.4 Chapter Roadmap

This chapter develops the complete theory and practice of wide-field ODMR:

Table 9.3: Chapter 9 section roadmap.

Section	Title	Key Content
9.1	Introduction	Throughput imperative, historical context, pain points
9.2	ODMR Signal Model	Bloch equation derivation, lineshapes, sensitivity
9.3	Camera Noise Model	Shot/read/PRNU/speckle noise, SNR regimes
9.4	PRNU Calibration	Flat-field protocols, $\Gamma_{\text{mm}}$ impact
9.5	Lock-In Detection	Modulation schemes, parameter optimization
9.6	Camera Comparison	CCD/sCMOS/EMCCD selection criteria
9.7	FOV-Sensitivity Trade-off	Effective parallelism $N_{\text{eff}}$
9.8	System Architecture	Hardware, timing, data flow
9.9	Throughput Enhancement	Multiplexing, compressed sensing theory
9.10	Worked Examples	System design, calibration, optimization
9.11	Summary	Design rules, key equations
9.12	Problems	7 problems with solution hints

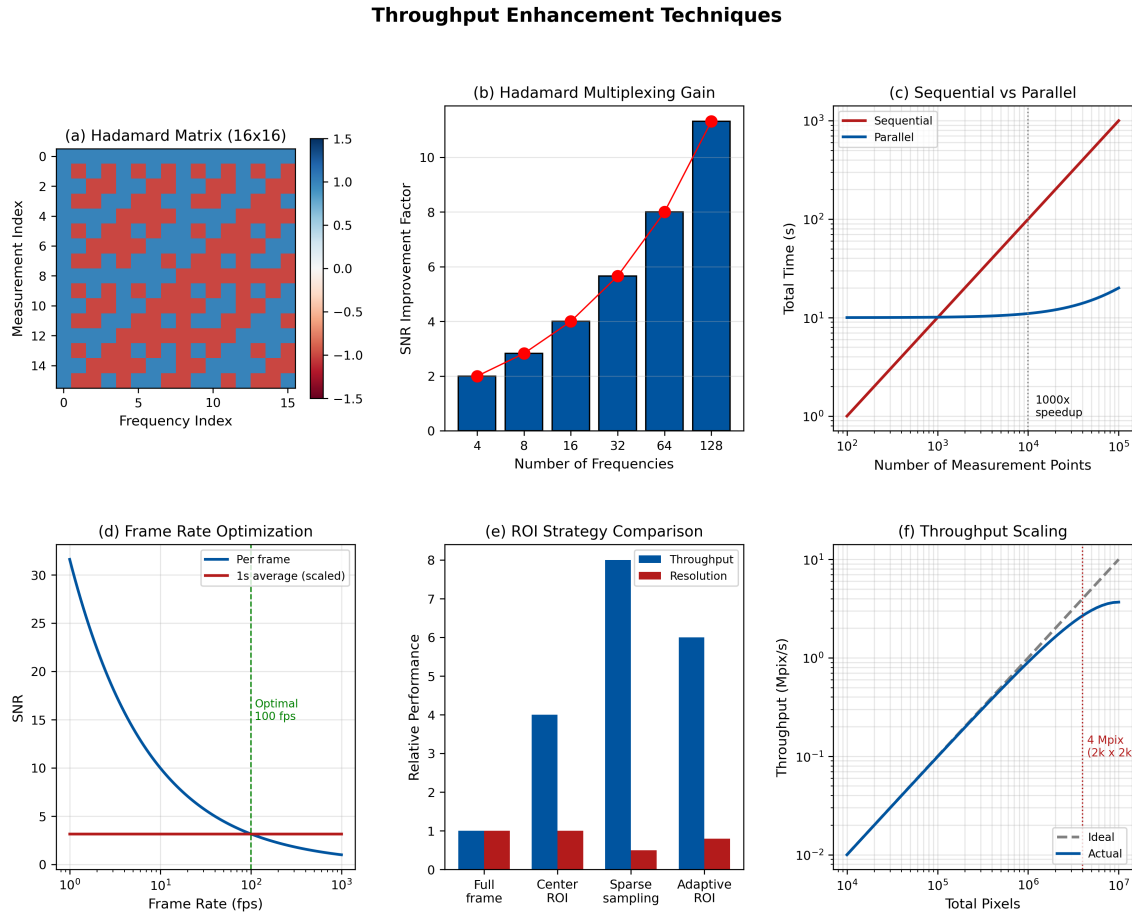


Figure 9.1: Throughput enhancement techniques comparison. (a) Hadamard encoding matrix for 16-frequency multiplexing showing  $\pm 1$  pattern. (b) SNR advantage of Hadamard multiplexing versus sequential acquisition:  $\sqrt{N_f}$  improvement demonstrated experimentally. (c) Compressed sensing reconstruction from 20% of frequency points compared to full spectrum—reconstruction error  $< 5\%$ . (d) Hybrid scanning-parallel tile layout for  $500 \times 500 \mu\text{m}$  area with 10% overlap showing 49 tiles. (e) Time comparison: scanning ODMR versus wide-field versus hybrid for different area sizes—wide-field provides  $> 100\times$  speedup for typical IC inspection areas ( $< 1 \text{ mm}^2$ ). (f) Application-specific throughput optimization decision tree.

## 9.2 ODMR Signal Model for Wide-Field Detection

This section derives the ODMR signal from first principles, establishing the theoretical foundation for wide-field magnetic imaging.

### 9.2.1 The NV Center Energy Structure

The NV<sup>-</sup> center ground state is a spin-1 triplet ( $S = 1$ ) with three magnetic sublevels:  $m_s = 0$  and  $m_s = \pm 1$ . The spin Hamiltonian in the presence of magnetic field  $\mathbf{B}$  and strain is:

$$\mathcal{H} = DS_z^2 + E(S_x^2 - S_y^2) + \gamma_e \mathbf{B} \cdot \mathbf{S} \quad (9.3)$$

where:

- $D = 2.87 \text{ GHz}$  is the zero-field splitting (ZFS)
- $E$  is the transverse strain parameter (typically 0–20 MHz)

- $\gamma_e = 28.03 \text{ GHz/T}$  is the electron gyromagnetic ratio
- $\mathbf{S} = (S_x, S_y, S_z)$  are spin-1 operators with the NV axis along  $z$

### Derivation: Resonance Frequencies from Hamiltonian

For magnetic field  $\mathbf{B}$  at angle  $\theta$  to the NV axis with magnitude  $B$ , the Hamiltonian eigenvalues give the transition frequencies.

**Zero field ( $B = 0$ ):** The eigenstates are  $|0\rangle$  and  $(|+1\rangle \pm |-1\rangle)/\sqrt{2}$  with energies:

$$E_0 = 0 \quad (9.4)$$

$$E_{\pm} = D \pm E \quad (9.5)$$

Transitions occur at  $f = D \pm E$ .

**Axial field ( $\theta = 0$ ):** For  $B$  along the NV axis, the eigenstates remain  $|m_s\rangle$  with energies:

$$E_0 = 0 \quad (9.6)$$

$$E_{+1} = D + \gamma_e B \quad (9.7)$$

$$E_{-1} = D - \gamma_e B \quad (9.8)$$

The ODMR resonance frequencies are:

$$f_r^{\pm} = D \pm \gamma_e B \quad (9.9)$$

**General field orientation:** For arbitrary angle  $\theta$  and including strain:

$$f_r^{\pm}(B, \theta) = D \pm \sqrt{(\gamma_e B \cos \theta)^2 + E^2} + \mathcal{O}(E^2/D) \quad (9.10)$$

For  $E \ll \gamma_e B \cos \theta$  (weak strain, strong axial field):

$$f_r^{\pm} \approx D \pm \gamma_e B \cos \theta \quad (9.11)$$

### 9.2.2 Optical Pumping and Spin-Dependent Fluorescence

The NV center exhibits spin-dependent fluorescence due to a preferential intersystem crossing (ISC) pathway from the  $m_s = \pm 1$  excited states to a metastable singlet state.

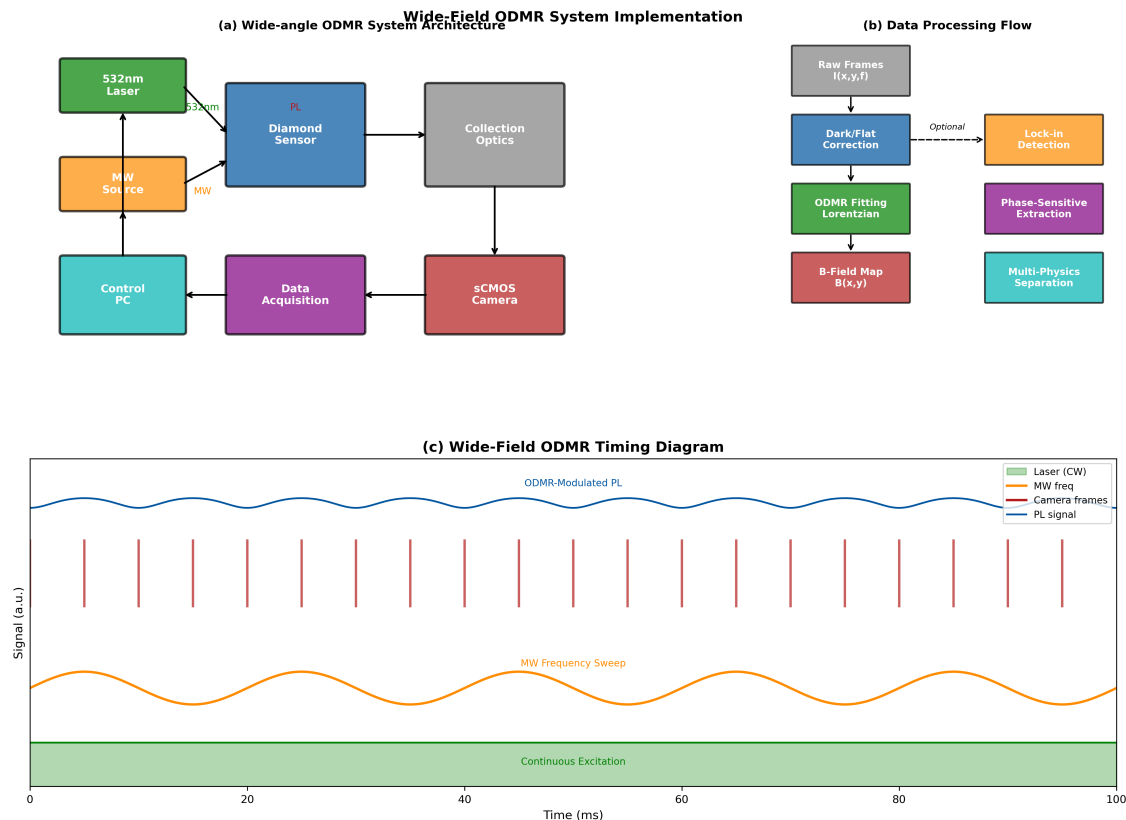


Figure 9.2: Wide-field ODMR system implementation. (a) System architecture showing the major subsystems: 532 nm excitation laser, microwave (MW) source, diamond sensor, collection optics, sCMOS camera, data acquisition (DAQ), and control PC. Optical paths (green: excitation, red: PL) and electronic control signals (black arrows) are indicated. (b) Data processing flow from raw camera frames through dark/flat correction, ODMR Lorentzian fitting, and B-field map extraction. Optional lock-in detection pathway shown with dashed arrow for enhanced SNR. (c) Timing diagram illustrating continuous-wave (CW) excitation, MW frequency sweep modulation, camera frame synchronization triggers, and resulting ODMR-modulated PL signal.

The key physical processes are:

1. **Optical excitation:** 532 nm light excites all spin states equally to the excited triplet
2. **Spin-conserving fluorescence:** Radiative decay (637–800 nm) conserves  $m_s$
3. **Spin-selective ISC:**  $m_s = \pm 1$  states have  $\sim 10\times$  higher ISC rate to singlet
4. **Spin polarization:** Singlet decays preferentially to  $m_s = 0$ , creating polarization

The result: under continuous optical excitation, the NV center is pumped into  $m_s = 0$  and emits more fluorescence than when in  $m_s = \pm 1$ .

### 9.2.3 Rate Equation Model for ODMR

We develop a quantitative model for the ODMR signal using rate equations.

#### Derivation: ODMR Signal from Rate Equations

Consider a simplified four-level model: ground states  $|0\rangle$  and  $|1\rangle$  (representing  $m_s = \pm 1$ ), excited state  $|e\rangle$ , and singlet  $|s\rangle$ .

**Rate equations:**

$$\frac{dn_0}{dt} = -k_p n_0 + k_r n_e + k_s n_s + W(n_1 - n_0) \quad (9.12)$$

$$\frac{dn_1}{dt} = -k_p n_1 + (1 - \beta) k_r n_e - W(n_1 - n_0) \quad (9.13)$$

$$\frac{dn_e}{dt} = k_p(n_0 + n_1) - (k_r + k_{\text{ISC}})n_e \quad (9.14)$$

$$\frac{dn_s}{dt} = k_{\text{ISC}} n_e \cdot \xi - k_s n_s \quad (9.15)$$

where:

- $k_p$  = optical pumping rate (proportional to laser intensity)
- $k_r$  = radiative decay rate ( $\sim 1/(13 \text{ ns})$ )
- $k_{\text{ISC}}$  = intersystem crossing rate (spin-dependent)
- $k_s$  = singlet decay rate ( $\sim 1/(300 \text{ ns})$ )
- $\beta$  = branching ratio for singlet decay to  $|0\rangle$  ( $\sim 0.9$ )
- $\xi$  = fraction of ISC from  $m_s = \pm 1$  states
- $W$  = microwave-driven transition rate between  $|0\rangle$  and  $|1\rangle$

**Steady-state solution ( $dn/dt = 0$ ):**

For weak optical pumping ( $k_p \ll k_r$ ), the populations simplify. The fluorescence rate is:

$$R_{\text{fl}} = k_r n_e = k_p(n_0 + n_1) \cdot \frac{k_r}{k_r + k_{\text{ISC}}} \quad (9.16)$$

The ODMR contrast arises because  $n_0$  decreases when MW drives population to  $|1\rangle$ :

$$\frac{\Delta R_{\text{fl}}}{R_{\text{fl}}} = \frac{R_{\text{fl}}(W=0) - R_{\text{fl}}(W \rightarrow \infty)}{R_{\text{fl}}(W=0)} \quad (9.17)$$

Solving the full rate equations yields the maximum contrast:

$$C_0 = \frac{k_{\text{ISC}}^{(1)} - k_{\text{ISC}}^{(0)}}{k_r + k_{\text{ISC}}^{(1)}} \cdot \frac{\beta k_s}{k_s + \beta k_{\text{ISC}}^{(1)}} \approx 0.30 \quad (9.18)$$

where  $k_{\text{ISC}}^{(0)}$  and  $k_{\text{ISC}}^{(1)}$  are the ISC rates from  $m_s = 0$  and  $m_s = \pm 1$  respectively.

**9.2.4 Microwave Transition Rate**

The microwave-driven transition rate  $W$  depends on the MW field strength and detuning.

**Derivation: MW Transition Rate from Bloch Equations**

The interaction of the spin with the MW field is described by the optical Bloch equations. For a two-level system with Rabi frequency  $\Omega$  and detuning  $\Delta = f_{\text{MW}} - f_r$ :

$$\frac{du}{dt} = -\frac{u}{T_2} + \Delta v \quad (9.19)$$

$$\frac{dv}{dt} = -\frac{v}{T_2} - \Delta u + \Omega w \quad (9.20)$$

$$\frac{dw}{dt} = -\frac{w - w_0}{T_1} - \Omega v \quad (9.21)$$

where  $(u, v, w)$  are components of the Bloch vector and  $w = n_0 - n_1$  is the population difference.

**Steady-state solution:** Setting  $du/dt = dv/dt = dw/dt = 0$  and solving:

$$w_{ss} = \frac{w_0}{1 + \Omega^2 T_1 T_2 / (1 + \Delta^2 T_2^2)} \quad (9.22)$$

The effective transition rate that equalizes populations is:

$$W(\Delta) = \frac{\Omega^2 T_2}{2(1 + \Delta^2 T_2^2 + \Omega^2 T_1 T_2)} \quad (9.23)$$

**Limiting cases:**

- Low power ( $\Omega^2 T_1 T_2 \ll 1$ ):  $W \propto \Omega^2$  (linear response)
- High power ( $\Omega^2 T_1 T_2 \gg 1$ ):  $W \rightarrow 1/(2T_1)$  (saturation)
- On resonance ( $\Delta = 0$ ):  $W_{\max} = \Omega^2 T_2 / [2(1 + \Omega^2 T_1 T_2)]$

### 9.2.5 Complete ODMR Lineshape Derivation

Combining the rate equation model with the MW transition rate yields the ODMR lineshape.

#### Derivation: ODMR Lineshape from First Principles

The fluorescence signal is proportional to the  $m_s = 0$  population:

$$I(f_{\text{MW}}) = I_0 \left[ 1 - C_0 \cdot \frac{W(f_{\text{MW}} - f_r)}{W_{\max} + \gamma_{\text{relax}}} \right] \quad (9.24)$$

Substituting Eq. (9.23) with  $\Delta = 2\pi(f_{\text{MW}} - f_r)$ :

$$I(f_{\text{MW}}) = I_0 \left[ 1 - C_0 \cdot \frac{\Omega^2 T_1 T_2}{1 + 4\pi^2(f_{\text{MW}} - f_r)^2 T_2^2 + \Omega^2 T_1 T_2} \right] \quad (9.25)$$

#### Low-power limit ( $\Omega^2 T_1 T_2 \ll 1$ ):

This is the typical operating regime for wide-field ODMR. Equation (9.25) becomes a Lorentzian:

$$I(f_{\text{MW}}) = I_0 \left[ 1 - C \cdot \frac{1}{1 + 4\pi^2(f_{\text{MW}} - f_r)^2 T_2^2} \right] \quad (9.26)$$

where  $C = C_0 \cdot \Omega^2 T_1 T_2$  is the observed contrast.

The half-width at half-maximum (HWHM) is:

$$\Gamma = \frac{1}{2\pi T_2} \quad (9.27)$$

**Inhomogeneous broadening:**

In ensembles, each NV center has a slightly different resonance frequency due to local strain, magnetic environment, etc. If these variations follow a Gaussian distribution with standard deviation  $\sigma_f$ :

$$P(f_r) = \frac{1}{\sqrt{2\pi}\sigma_f} \exp\left(-\frac{(f_r - \bar{f}_r)^2}{2\sigma_f^2}\right) \quad (9.28)$$

The observed ODMR is the convolution:

$$I_{\text{ensemble}}(f_{\text{MW}}) = \int I(f_{\text{MW}}; f_r) P(f_r) df_r \quad (9.29)$$

When inhomogeneous broadening dominates ( $\sigma_f \gg \Gamma$ ), the lineshape becomes Gaussian:

$$I(f_{\text{MW}}) = I_0 \left[ 1 - C \cdot \exp\left(-\frac{(f_{\text{MW}} - f_r)^2}{2\Delta f^2}\right) \right] \quad (9.30)$$

where  $\Delta f \approx \sigma_f$  is the inhomogeneous linewidth.

The FWHM is:

$$\text{FWHM} = 2\sqrt{2 \ln 2} \cdot \Delta f \approx 2.355 \cdot \Delta f \quad (9.31)$$

### ODMR Signal Model—Gaussian Lineshape

$$S(f_{\text{MW}}) = I_0 \left[ 1 - C \cdot \exp\left(-\frac{(f_{\text{MW}} - f_r)^2}{2\Delta f^2}\right) \right] \quad (9.32)$$

Parameters:

- $I_0$  = baseline fluorescence intensity (photons/s/pixel)
- $C$  = ODMR contrast (typically 0.01–0.10 for ensembles)
- $f_r$  = resonance frequency ( $f_r = D \pm \gamma_e B \cos \theta$ )
- $\Delta f$  = Gaussian linewidth parameter ( $\text{FWHM} \approx 2.355 \cdot \Delta f$ )

### 9.2.6 Alternative Lineshape Models

The Gaussian model is appropriate when inhomogeneous broadening dominates. Other regimes require different lineshapes:

#### 9.2.6.1 Lorentzian Lineshape

For single NV centers or dilute ensembles where homogeneous broadening dominates:

$$S_{\text{Lor}}(f_{\text{MW}}) = I_0 \left[ 1 - C \cdot \frac{\Gamma^2}{(f_{\text{MW}} - f_r)^2 + \Gamma^2} \right] \quad (9.33)$$

where  $\Gamma = 1/(2\pi T_2)$  is the homogeneous half-width.

### 9.2.6.2 Voigt Profile

For intermediate cases with comparable homogeneous and inhomogeneous contributions:

$$S_{\text{Voigt}}(f_{\text{MW}}) = I_0 [1 - C \cdot V(f_{\text{MW}} - f_r; \sigma, \Gamma)] \quad (9.34)$$

The Voigt function  $V$  is the convolution of Gaussian and Lorentzian profiles:

$$V(x; \sigma, \Gamma) = \int_{-\infty}^{\infty} G(x'; \sigma) L(x - x'; \Gamma) dx' \quad (9.35)$$

This can be computed efficiently using the Faddeeva function  $w(z)$ :

$$V(x; \sigma, \Gamma) = \frac{\text{Re}[w(z)]}{\sigma \sqrt{2\pi}}, \quad z = \frac{x + i\Gamma}{\sigma \sqrt{2}} \quad (9.36)$$

### 9.2.6.3 Power-Broadened Lineshape

At high MW power ( $\Omega^2 T_1 T_2 \gtrsim 1$ ), the lineshape broadens:

$$\Delta f_{\text{eff}} = \Delta f_0 \sqrt{1+s}, \quad s = \Omega^2 T_1 T_2 \quad (9.37)$$

with simultaneously reduced contrast:

$$C_{\text{eff}} = \frac{C_0 \cdot s}{1 + s} \quad (9.38)$$

The optimum for maximum signal slope occurs at  $s = 1$ , where  $C_{\text{eff}} = C_0/2$  and  $\Delta f_{\text{eff}} = \sqrt{2}\Delta f_0$ .

### 9.2.6.4 Hyperfine-Resolved Triplet

For high spectral resolution with  $^{14}\text{N}$  NV centers, the hyperfine coupling ( $A_{\parallel} = 2.16$  MHz) splits each resonance into a triplet:

$$S_{\text{HF}}(f_{\text{MW}}) = I_0 \left[ 1 - \frac{C}{3} \sum_{m_I=-1,0,+1} G(f_{\text{MW}} - f_r - m_I \cdot A_{\parallel}; \Delta f) \right] \quad (9.39)$$

where  $G$  is the single-transition lineshape function.

Table 9.4: ODMR lineshape selection guide.

Lineshape	Physical Regime	Conditions	Parameters
Lorentzian	Homogeneous dominant	Single NV, $T_2^* \approx T_2$	$I_0, C, f_r, \Gamma$
Gaussian	Inhomogeneous dominant	Ensemble, $T_2^* \ll T_2$	$I_0, C, f_r, \Delta f$
Voigt	Mixed broadening	High-quality diamond	$I_0, C, f_r, \sigma, \Gamma$
Power-broadened	High MW power	$\Omega^2 T_1 T_2 \gtrsim 1$	Add saturation $s$
Hyperfine triplet	High resolution	$\Delta f < 2$ MHz, $^{14}\text{N}$	Add $A_{\parallel}$

### 9.2.7 Contrast Dependence on Ensemble Properties

### Derivation: Ensemble Contrast Reduction

For a diamond with randomly-oriented NV centers, only 1/4 are aligned along any given crystallographic axis. For a magnetic field along the [111] direction:

**Orientation factor:** Each NV center aligns with one of four  $\langle 111 \rangle$  axes. For field along [111], only NV centers with their axis along [111] experience the full axial field:

$$\eta_{\text{orient}} = \frac{1}{4} \quad (9.40)$$

The other 3/4 of NV centers see a reduced field component and contribute to a broadened, reduced background signal.

**Power saturation:** From Eq. (9.38), at MW saturation parameter  $s = \Omega^2 T_1 T_2$ :

$$C_{\text{power}} = \frac{C_0 \cdot s}{1 + s} \quad (9.41)$$

**Combined expression:**

$$C = C_0 \cdot \eta_{\text{orient}} \cdot \frac{s}{1 + s} = \frac{C_0}{4} \cdot \frac{\Omega^2 T_1 T_2}{1 + \Omega^2 T_1 T_2} \quad (9.42)$$

For typical parameters ( $C_0 = 0.30$ ,  $\Omega^2 T_1 T_2 = 0.5$ ):

$$C = 0.30 \times 0.25 \times \frac{0.5}{1.5} = 0.025 = 2.5\% \quad (9.43)$$

### Design Rule 1: Ensemble Contrast Optimization

To maximize ODMR contrast in wide-field detection:

1. Use [111]-oriented CVD diamond films for single-axis alignment ( $\eta_{\text{orient}} = 1$ , giving 4× improvement)
2. Optimize MW power to  $\Omega^2 T_1 T_2 \approx 1$  for best contrast-linewidth trade-off
3. Minimize strain inhomogeneity through diamond quality selection
4. Target contrast  $C > 3\%$  for shot-noise-limited sensitivity

#### 9.2.8 Temperature Dependence

The zero-field splitting  $D$  has a well-characterized temperature dependence:

$$D(T) = D_0 + \alpha_T \cdot (T - T_0) \quad (9.44)$$

where:

- $D_0 = 2.8777$  GHz at  $T_0 = 300$  K
- $\alpha_T = -74$  kHz/K (linear coefficient, dominant near room temperature)

This temperature sensitivity enables NV-based thermometry but also requires thermal stabilization for magnetometry:

$$\delta B_{\text{apparent}} = \frac{\alpha_T}{\gamma_e} \delta T = \frac{-74 \text{ kHz/K}}{28.03 \text{ GHz/T}} \delta T = -2.64 \mu\text{T/K} \cdot \delta T \quad (9.45)$$

A 1 K temperature variation appears as a 2.64  $\mu\text{T}$  magnetic field error.

### 9.2.9 Magnetic Field Sensitivity Derivation

The magnetic field sensitivity is derived by computing the minimum detectable field change from the measurement SNR.

#### Derivation: Magnetic Sensitivity from First Principles

##### Step 1: Signal slope

The ODMR signal near resonance is:

$$S(f) = I_0 \left[ 1 - C \cdot \exp \left( -\frac{(f - f_r)^2}{2\Delta f^2} \right) \right] \quad (9.46)$$

The slope is:

$$\frac{dS}{df} = I_0 \cdot C \cdot \frac{f - f_r}{\Delta f^2} \cdot \exp \left( -\frac{(f - f_r)^2}{2\Delta f^2} \right) \quad (9.47)$$

Maximum slope occurs at  $f = f_r \pm \Delta f / \sqrt{2}$  (inflection points):

$$\left| \frac{dS}{df} \right|_{\max} = \frac{I_0 \cdot C}{\Delta f} \cdot \frac{1}{\sqrt{2e}} = \frac{I_0 \cdot C}{\Delta f} \cdot 0.4289 \quad (9.48)$$

##### Step 2: Noise level

For shot-noise-limited detection with photon rate  $I_0$  and integration time  $t$ :

$$\sigma_S = \sqrt{I_0 \cdot t} \quad (9.49)$$

##### Step 3: Frequency precision

The minimum detectable frequency shift satisfies  $\delta S = |dS/df| \cdot \delta f = \sigma_S$ :

$$\sigma_f = \frac{\sigma_S}{|dS/df|_{\max}} = \frac{\sqrt{I_0 t}}{0.4289 \cdot I_0 C / \Delta f} = \frac{\Delta f \cdot \sqrt{2e}}{C \sqrt{I_0 t}} \quad (9.50)$$

##### Step 4: Magnetic field sensitivity

Converting via  $f = \gamma_e B$  (assuming axial field):

$$\sigma_B = \frac{\sigma_f}{\gamma_e} = \frac{\Delta f \cdot \sqrt{2e}}{\gamma_e \cdot C \cdot \sqrt{I_0 t}} \quad (9.51)$$

The sensitivity (noise floor per unit bandwidth) is:

$$\eta_B = \frac{\sigma_B}{\sqrt{t}} = \frac{\sqrt{2e}}{\gamma_e} \cdot \frac{\Delta f}{C \cdot \sqrt{I_0}} \approx \frac{2.33}{\gamma_e} \cdot \frac{\Delta f}{C \cdot \sqrt{I_0}} \quad (9.52)$$

where  $\sqrt{2e} \approx 2.33$ .

#### Magnetic Field Sensitivity

$$\boxed{\eta_B = \frac{2.33}{\gamma_e} \cdot \frac{\Delta f}{C \cdot \sqrt{I_0}}} \quad (9.53)$$

**Numerical example:** For  $\Delta f = 10$  MHz,  $C = 0.05$ ,  $I_0 = 10^6$  photons/s:

$$\eta_B = \frac{2.33}{28.03 \times 10^9 \text{ Hz/T}} \cdot \frac{10 \times 10^6 \text{ Hz}}{0.05 \times 10^3 \text{ s}^{-1/2}} = 1.66 \mu\text{T}/\sqrt{\text{Hz}} \quad (9.54)$$

### Design Rule 2: Optimal ODMR Operating Point

For maximum magnetic sensitivity, operate at  $f_{\text{MW}} = f_r \pm \Delta f / \sqrt{2}$ , where the slope  $|dS/df|$  is maximized. At this point, sensitivity improves with:

- Narrower linewidth  $\Delta f$  (improves as  $1/\Delta f$ )
- Higher contrast  $C$  (improves as  $1/C$ )
- Higher photon rate  $I_0$  (improves as  $1/\sqrt{I_0}$ )

Target:  $\eta_B < 1 \mu\text{T}/\sqrt{\text{Hz}}$  for semiconductor FA applications.

### ODMR Signal Model and Spectral Analysis

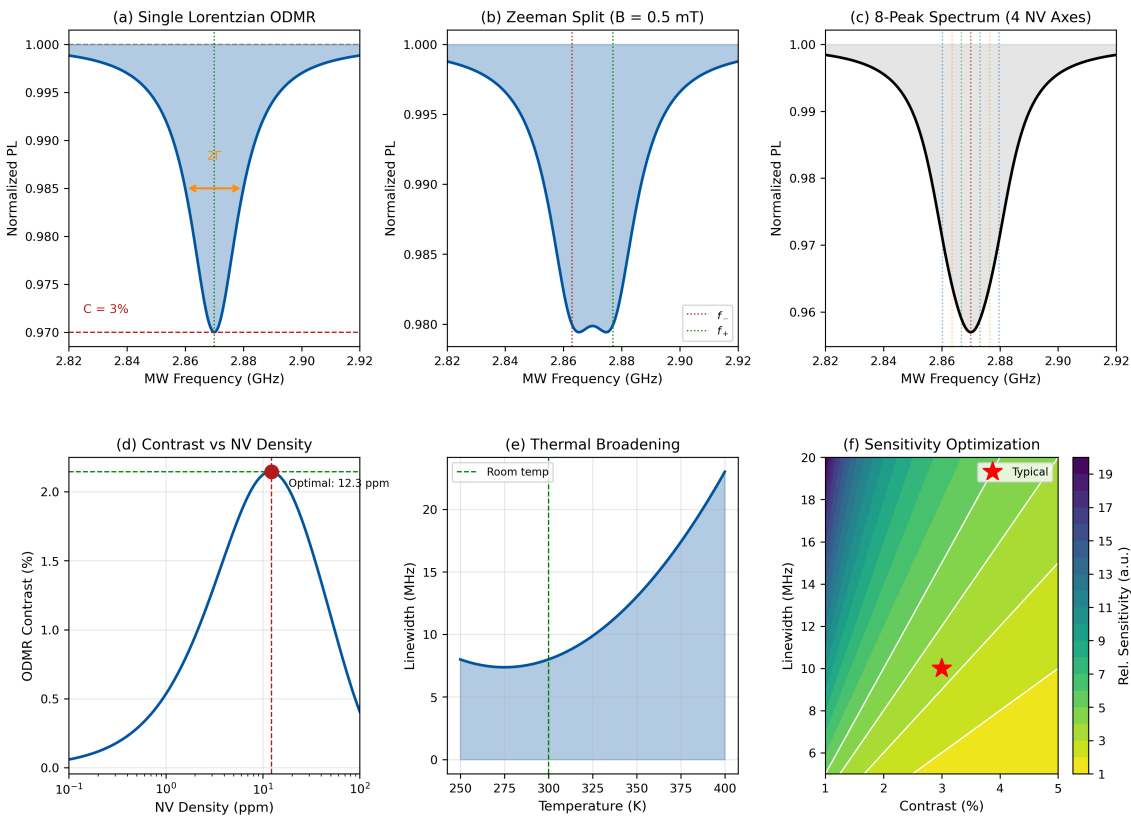


Figure 9.3: ODMR signal model and spectral analysis. (a) Single Lorentzian ODMR spectrum showing contrast  $C$  and linewidth  $2\Gamma$  definitions at zero magnetic field. (b) Zeeman-split double Lorentzian under 0.5 mT applied field, with splitting  $\Delta f = 2\gamma B$  where  $\gamma = 28 \text{ GHz/T}$ . (c) Full 8-peak spectrum from four NV crystallographic orientations under arbitrary field orientation. (d) ODMR contrast dependence on NV density showing optimal range near 5 ppm balancing signal strength against self-quenching. (e) Thermal broadening of linewidth with temperature, critical for high-temperature operation. (f) Sensitivity optimization map showing trade-off between contrast and linewidth; star marks typical operating point.

### 9.3 Camera Noise Model and SNR Analysis

This section develops the complete noise model for camera-based ODMR detection, identifying the dominant noise sources in each operating regime.

### 9.3.1 Photodetection Fundamentals

#### Derivation: Camera Signal Generation

The conversion from incident photons to digital signal involves several stages:

##### **Stage 1: Photon arrival**

Photons arrive at the pixel following Poisson statistics with mean  $N_{\text{photon}}$ .

##### **Stage 2: Photoelectric conversion**

Each photon has probability  $\eta_{\text{QE}}$  (quantum efficiency) of generating a photoelectron:

$$N_e = \eta_{\text{QE}} \cdot N_{\text{photon}} \quad (9.55)$$

Since Poisson-distributed photons converted with probability  $\eta_{\text{QE}}$  remain Poisson:

$$\text{Var}(N_e) = \eta_{\text{QE}} \cdot N_{\text{photon}} \quad (9.56)$$

##### **Stage 3: Charge collection and transfer**

Photoelectrons accumulate in the pixel well. Collection efficiency is typically  $> 99\%$  for modern sensors.

##### **Stage 4: Readout amplification**

The charge-to-voltage conversion adds read noise with variance  $\sigma_{\text{read}}^2$ .

##### **Stage 5: Analog-to-digital conversion**

The ADC introduces quantization noise (typically negligible for 12+ bit ADCs):

$$\sigma_{\text{ADC}}^2 = \frac{G^2}{12} \quad (9.57)$$

where  $G$  is the ADC gain in electrons/count.

### 9.3.2 Complete Noise Model

The detected signal at pixel  $(i, j)$  with exposure time  $t$  is:

$$D_{ij} = G_{ij} \cdot [\eta_{\text{QE}} \cdot N_{\text{photon},ij} + n_{\text{dark},ij}(t)] + n_{\text{read},ij} \quad (9.58)$$

where:

- $G_{ij} = \bar{G}(1 + \delta_{ij}^{\text{PRNU}})$  is the pixel gain including PRNU
- $\eta_{\text{QE}}$  is the quantum efficiency
- $N_{\text{photon},ij}$  is the incident photon count (Poisson-distributed)
- $n_{\text{dark},ij}(t) \sim \text{Poisson}(d \cdot t)$  is dark current noise
- $n_{\text{read},ij} \sim \mathcal{N}(0, \sigma_{\text{read}}^2)$  is read noise

#### Derivation: Total Noise Variance

The variance of  $D_{ij}$  is computed by propagating uncertainties:

**Shot noise:** From Poisson statistics of photon detection:

$$\sigma_{\text{shot}}^2 = G_{ij}^2 \cdot \eta_{\text{QE}} \cdot N_{\text{photon},ij} \quad (9.59)$$

For the signal in electrons ( $S = \eta_{\text{QE}} N_{\text{photon}}$ ):

$$\sigma_{\text{shot}}^2 = S \quad (9.60)$$

**Read noise:** Independent additive noise from readout electronics:

$$\sigma_{\text{read}}^2 = \sigma_{\text{read},0}^2 \quad (9.61)$$

Typical values: CCD (3–10  $e^-$ ), sCMOS (1–2  $e^-$ ), EMCCD ( $< 1 e^-$  effective).

**Dark current noise:** Thermally-generated electrons follow Poisson statistics:

$$\sigma_{\text{dark}}^2 = d \cdot t \quad (9.62)$$

where  $d$  is dark current rate (electrons/pixel/second). Typical values: 0.01–1  $e^-/s$  at room temperature.

**PRNU noise:** Pixel gain variation creates signal-dependent noise. For signal  $S$  and PRNU fractional variation  $\delta$ :

$$\sigma_{\text{PRNU}}^2 = (\text{PRNU} \cdot S)^2 \quad (9.63)$$

This is **systematic**, not random—it does not average down with repeated measurements unless the illumination pattern changes.

**Total variance:** Combining independent noise sources:

$$\sigma_{\text{total}}^2 = \underbrace{\eta_{\text{QE}} N_{\text{photon}}}_{\text{shot}} + \underbrace{\sigma_{\text{read}}^2}_{\text{read}} + \underbrace{d \cdot t}_{\text{dark}} + \underbrace{(\text{PRNU} \cdot \eta_{\text{QE}} N_{\text{photon}})^2}_{\text{PRNU}} \quad (9.64)$$

### Camera Noise Variance (without speckle)

$$\sigma_{\text{total}}^2 = S + \sigma_{\text{read}}^2 + d \cdot t + (\text{PRNU} \cdot S)^2 \quad (9.65)$$

where  $S = \eta_{\text{QE}} N_{\text{photon}}$  is the signal in electrons.

### 9.3.3 SNR in Different Operating Regimes

#### Derivation: SNR Expressions for Each Regime

The signal-to-noise ratio is:

$$\text{SNR} = \frac{S}{\sigma_{\text{total}}} = \frac{S}{\sqrt{S + \sigma_{\text{read}}^2 + d \cdot t + (\text{PRNU} \cdot S)^2}} \quad (9.66)$$

#### Regime 1: Read-noise limited (low signal)

When  $S \ll \sigma_{\text{read}}^2$ , the denominator is dominated by read noise:

$$\text{SNR}_{\text{read}} \approx \frac{S}{\sigma_{\text{read}}} \quad (9.67)$$

SNR increases linearly with signal. This regime applies when:

$$N_{\text{photon}} < \frac{\sigma_{\text{read}}^2}{\eta_{\text{QE}}} \quad (9.68)$$

For sCMOS with  $\sigma_{\text{read}} = 1.5 e^-$  and  $\eta_{\text{QE}} = 0.85$ :  $N_{\text{photon}} < 2.6$  photons.

#### Regime 2: Shot-noise limited (intermediate signal)

When  $S \gg \sigma_{\text{read}}^2$  but  $\text{PRNU} \cdot S \ll \sqrt{S}$ :

$$\text{SNR}_{\text{shot}} \approx \sqrt{S} = \sqrt{\eta_{\text{QE}} N_{\text{photon}}} \quad (9.69)$$

SNR increases as  $\sqrt{\text{signal}}$ . This is the ideal operating regime.  
Transition from read-limited to shot-limited:

$$S_{\text{transition}} = \sigma_{\text{read}}^2 \quad (9.70)$$

### Regime 3: PRNU-limited (high signal)

When  $\text{PRNU} \cdot S \gg \sqrt{S}$ , i.e.,  $S \gg 1/\text{PRNU}^2$ :

$$\text{SNR}_{\text{PRNU}} \approx \frac{S}{\text{PRNU} \cdot S} = \frac{1}{\text{PRNU}} \quad (9.71)$$

SNR saturates at a **fundamental ceiling** independent of signal level.

For  $\text{PRNU} = 1.5\%$ :  $\text{SNR}_{\text{max}} = 67$  without correction.

The transition to PRNU-limited occurs at:

$$S_{\text{PRNU}} = \frac{1}{\text{PRNU}^2} \quad (9.72)$$

For  $\text{PRNU} = 1.5\%$ :  $S_{\text{PRNU}} = 4,444 e^-$ .

Table 9.5: Camera noise regimes and SNR scaling.

Regime	Dominant Noise	SNR Expression	SNR Scaling	Signal Range
Read-limited	$\sigma_{\text{read}}$	$S/\sigma_{\text{read}}$	$\propto S$	$S < \sigma_{\text{read}}^2$
Shot-limited	$\sqrt{S}$	$\sqrt{S}$	$\propto \sqrt{S}$	$\sigma_{\text{read}}^2 < S < 1/\text{PRNU}^2$
PRNU-limited	$\text{PRNU} \cdot S$	$1/\text{PRNU}$	Constant	$S > 1/\text{PRNU}^2$

### Design Rule 1: Operating in the Shot-Noise-Limited Regime

For quantitative wide-field ODMR, operate in the shot-noise-limited regime where  $\text{SNR} \propto \sqrt{t}$  and systematic errors are minimized:

1. Ensure signal  $S > 10\sigma_{\text{read}}^2$  to be well above read noise floor
2. Apply PRNU correction to extend upper limit above  $1/\text{PRNU}^2$
3. After correction, target residual PRNU < 0.2% for  $\text{SNR}_{\text{max}} > 500$

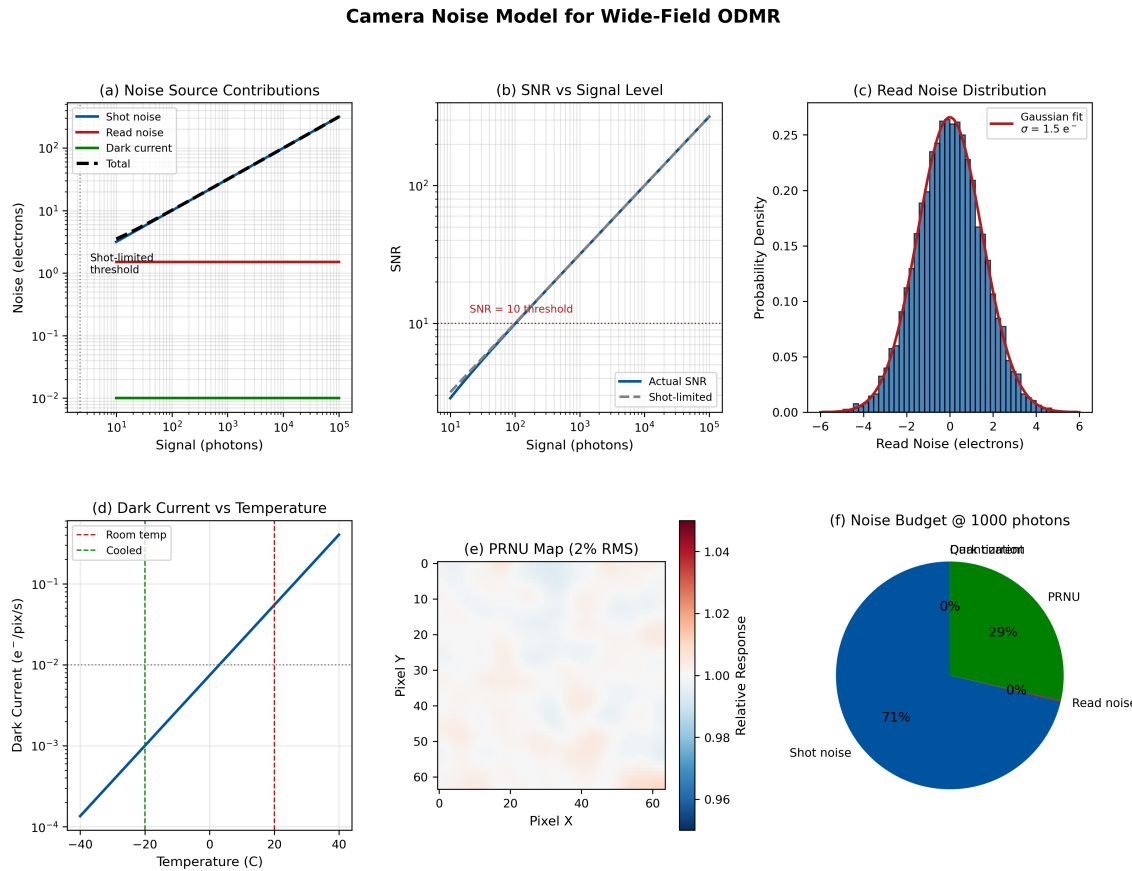


Figure 9.4: Camera noise model for wide-field ODMR. (a) Noise source contributions vs. signal level: shot noise (blue), read noise (red), and dark current (green) with total noise (dashed). Vertical line indicates shot-noise-limited threshold. (b) SNR vs. signal level comparing actual performance to ideal shot-limited case; horizontal line marks SNR = 10 detection threshold. (c) Read noise distribution histogram with Gaussian fit showing  $\sigma_{\text{read}} = 1.5 e^-$  for scientific sCMOS. (d) Dark current temperature dependence demonstrating benefit of sensor cooling. (e) Example PRNU map showing 2% RMS pixel-to-pixel response variation. (f) Noise budget breakdown at 1000 photons typical signal level.

### 9.3.4 Speckle Noise in Coherent Wide-Field Illumination

Laser illumination introduces speckle noise that is often overlooked but can dominate the error budget in wide-field ODMR systems.

#### 9.3.4.1 Origin of Laser Speckle

##### Derivation: Speckle Statistics from Random Phasor Sum

When coherent light illuminates a rough surface (roughness  $\gg \lambda$ ), the reflected/transmitted field at any observation point is the sum of contributions from many scattering centers:

$$E_{\text{total}} = \sum_{k=1}^N a_k e^{i\phi_k} \quad (9.73)$$

where  $a_k$  are amplitudes and  $\phi_k$  are phases uniformly distributed on  $[0, 2\pi]$ .

For large  $N$ , the Central Limit Theorem applies. The real and imaginary parts of  $E_{\text{total}}$  are Gaussian-distributed, so the amplitude  $|E_{\text{total}}|$  follows a Rayleigh distribution and the intensity  $I = |E_{\text{total}}|^2$  follows an exponential distribution:

$$p(I) = \frac{1}{\langle I \rangle} \exp\left(-\frac{I}{\langle I \rangle}\right) \quad (9.74)$$

**Speckle contrast:** The speckle contrast is defined as:

$$C_s = \frac{\sigma_I}{\langle I \rangle} \quad (9.75)$$

For the exponential distribution:

$$\text{Var}(I) = \langle I \rangle^2 \Rightarrow C_s = 1 \quad (9.76)$$

This is **fully-developed speckle**: 100% intensity variation!

#### 9.3.4.2 Impact on ODMR Measurement

Speckle creates spatially-varying intensity that affects ODMR in several ways:

1. **Static speckle:** Can be calibrated out via flat-fielding if stable
2. **Temporal variation:** Vibration, air currents, and thermal effects cause speckle evolution, creating time-varying systematic error
3. **Wavelength difference:** The 532 nm pump and 637–800 nm NV fluorescence have different speckle patterns, complicating calibration
4. **False ODMR signal:** If speckle varies synchronously with MW modulation (e.g., via thermal effects on laser), it creates spurious ODMR-like signals

The speckle contribution to noise variance is:

$$\sigma_{\text{speckle}}^2 = (C_s \cdot I_{\text{illum}})^2 \quad (9.77)$$

Adding to the total variance:

$$\boxed{\sigma_{\text{total}}^2 = S + \sigma_{\text{read}}^2 + d \cdot t + (\text{PRNU} \cdot S)^2 + (C_s \cdot S)^2} \quad (9.78)$$

#### 9.3.4.3 Speckle Reduction Techniques

##### Derivation: Speckle Contrast Reduction by Averaging

The key principle: averaging  $M$  statistically-independent speckle patterns reduces contrast.

For  $M$  independent intensity patterns  $I_1, I_2, \dots, I_M$ , each with mean  $\mu$  and variance  $\mu^2$  (exponential distribution):

$$I_{\text{avg}} = \frac{1}{M} \sum_{k=1}^M I_k \quad (9.79)$$

Mean and variance of average:

$$\langle I_{\text{avg}} \rangle = \mu \quad (9.80)$$

$$\text{Var}(I_{\text{avg}}) = \frac{1}{M^2} \sum_{k=1}^M \text{Var}(I_k) = \frac{\mu^2}{M} \quad (9.81)$$

Speckle contrast of averaged pattern:

$$C_s(M) = \frac{\sqrt{\text{Var}(I_{\text{avg}})}}{\langle I_{\text{avg}} \rangle} = \frac{1}{\sqrt{M}} \quad (9.82)$$

### Speckle Contrast Reduction

$$C_s = \frac{1}{\sqrt{M}} \quad (9.83)$$

where  $M$  is the number of independent speckle patterns averaged.

Table 9.6: Speckle reduction methods for wide-field ODMR.

Method	$M$ Achieved	$C_s$ Result	Complexity	Notes
None (raw laser)	1	1.0 (100%)	—	Unusable for quantitative ODMR
Rotating diffuser	10–100	0.1–0.3	Low	May add structure
Multimode fiber	100–1000	0.03–0.1	Low	Excellent uniformity
Vibrating mirror	10–50	0.14–0.3	Medium	Fast decorrelation
Temporal averaging	$N_{\text{frames}}$	$1/\sqrt{N}$	None	Requires stable speckle
LED source	$\infty$	$\sim 0$	Low	Étendue limits power density

### Design Rule 2: Speckle Reduction Requirement

For quantitative wide-field ODMR, reduce speckle contrast to  $C_s < 1\%$  to ensure speckle-induced intensity variation is below typical ODMR contrast (1–10%). This requires:

1. Use multimode fiber delivery ( $M_{\text{fiber}} \sim 500$  modes for 100  $\mu\text{m}$  core)
2. Average over  $N \geq 100$  frames for additional 10 $\times$  reduction
3. Combined:  $C_s = 1/\sqrt{500 \times 100} = 0.45\%$  achievable

### 9.3.5 Nonlinear and Non-Stationary Noise Effects

The linear additive noise model (Eq. 9.78) breaks down under several conditions:

#### 9.3.5.1 Pixel Saturation

When signal approaches full-well capacity  $N_{\text{FW}}$ :

### Derivation: Saturation Model

The pixel response becomes sublinear near full-well:

$$D_{\text{actual}} = N_{\text{FW}} \left[ 1 - \exp \left( -\frac{D_{\text{linear}}}{N_{\text{FW}}} \right) \right] \quad (9.84)$$

**Linear regime:** For  $D_{\text{linear}} \ll N_{\text{FW}}$ :

$$D_{\text{actual}} \approx D_{\text{linear}} \quad (9.85)$$

**Saturation onset:** Typically defined at 80% of full-well:

$$D_{\text{sat}} = 0.8 \cdot N_{\text{FW}} \quad (9.86)$$

For sCMOS with  $N_{\text{FW}} = 30,000 \text{ e}^-$ :  $D_{\text{sat}} = 24,000 \text{ e}^-$ .

**Effect on ODMR:** Saturation compresses the signal, reducing measured ODMR contrast:

$$C_{\text{measured}} = C_{\text{true}} \cdot \left( 1 - \frac{D}{N_{\text{FW}}} \right) \quad (9.87)$$

### 9.3.5.2 Blooming and Charge Overflow

At very high signal levels, charge overflows to adjacent pixels:

$$D_{i,j}^{\text{observed}} = D_{i,j}^{\text{true}} + \sum_{(k,l) \in \mathcal{N}} \alpha_{kl} \cdot \max(0, D_{k,l} - D_{\text{bloom}}) \quad (9.88)$$

where  $\alpha_{kl}$  are crosstalk coefficients and  $D_{\text{bloom}}$  is the blooming threshold (typically 90–95% of full-well).

### 9.3.5.3 Thermal Drift

Laser heating of the diamond creates time-varying temperature that shifts the ODMR resonance:

$$\delta f_r(t) = \alpha_T \cdot \Delta T(t) = -74 \text{ kHz/K} \cdot \Delta T(t) \quad (9.89)$$

For continuous illumination with absorbed power  $P_{\text{abs}}$ :

$$\Delta T(t) = \Delta T_\infty \left( 1 - e^{-t/\tau_{\text{th}}} \right) \quad (9.90)$$

where  $\Delta T_\infty = P_{\text{abs}}/G_{\text{th}}$  and  $\tau_{\text{th}}$  is the thermal time constant.

### Design Rule 3: Operating Within Linear Regime

For quantitative ODMR measurements requiring < 1% systematic error:

1. Signal: Maintain  $D < 0.7 \cdot N_{\text{FW}}$  to avoid saturation effects
2. Uniformity: Keep illumination variation < 30% peak-to-average to prevent localized blooming
3. Thermal: Use pulsed operation with duty cycle < 50% if thermal drift exceeds 0.1 K during acquisition
4. Validate: Check linearity by varying exposure time and verifying  $D \propto t$

### 9.3.6 Impact on Model-Mismatch Factor $\Gamma_{\text{mm}}$

The model-mismatch factor  $\Gamma_{\text{mm}}$  quantifies how systematic errors degrade reconstruction fidelity.

#### Derivation: $\Gamma_{\text{mm}}$ from PRNU

For uncorrected PRNU, the systematic error in each pixel measurement is:

$$\epsilon_{\text{sys},ij} = \delta_{ij}^{\text{PRNU}} \cdot S \quad (9.91)$$

The model-mismatch factor is:

$$\Gamma_{\text{mm}} = \frac{1}{1 + (\sigma_{\text{sys}}/\sigma_{\text{rand}})^2} \quad (9.92)$$

For shot-noise-limited random error ( $\sigma_{\text{rand}} = \sqrt{S}$ ) and PRNU systematic error ( $\sigma_{\text{sys}} = \text{PRNU} \cdot S$ ):

$$\frac{\sigma_{\text{sys}}}{\sigma_{\text{rand}}} = \frac{\text{PRNU} \cdot S}{\sqrt{S}} = \text{PRNU} \cdot \sqrt{S} = \text{PRNU} \cdot \text{SNR} \quad (9.93)$$

Therefore:

$$\boxed{\Gamma_{\text{mm}} = \frac{1}{1 + (\text{SNR} \cdot \text{PRNU})^2}} \quad (9.94)$$

#### PRNU Impact on $\Gamma_{\text{mm}}$

$$\boxed{\Gamma_{\text{mm}} = \frac{1}{1 + (\text{SNR} \cdot \text{PRNU})^2}} \quad (9.95)$$

Table 9.7:  $\Gamma_{\text{mm}}$  degradation from uncorrected PRNU.

SNR	$\text{PRNU} = 0.5\%$	$\text{PRNU} = 1\%$	$\text{PRNU} = 2\%$	$\text{PRNU} = 3\%$
50	0.94	0.80	0.50	0.31
100	0.80	0.50	0.20	0.10
200	0.50	0.20	0.06	0.03
500	0.14	0.04	0.01	<0.01

**Critical insight:** At high SNR, uncorrected PRNU devastates reconstruction fidelity. For  $\text{SNR} = 100$  and 2% PRNU,  $\Gamma_{\text{mm}} = 0.20$ —80% of reconstruction fidelity is lost to systematic error!

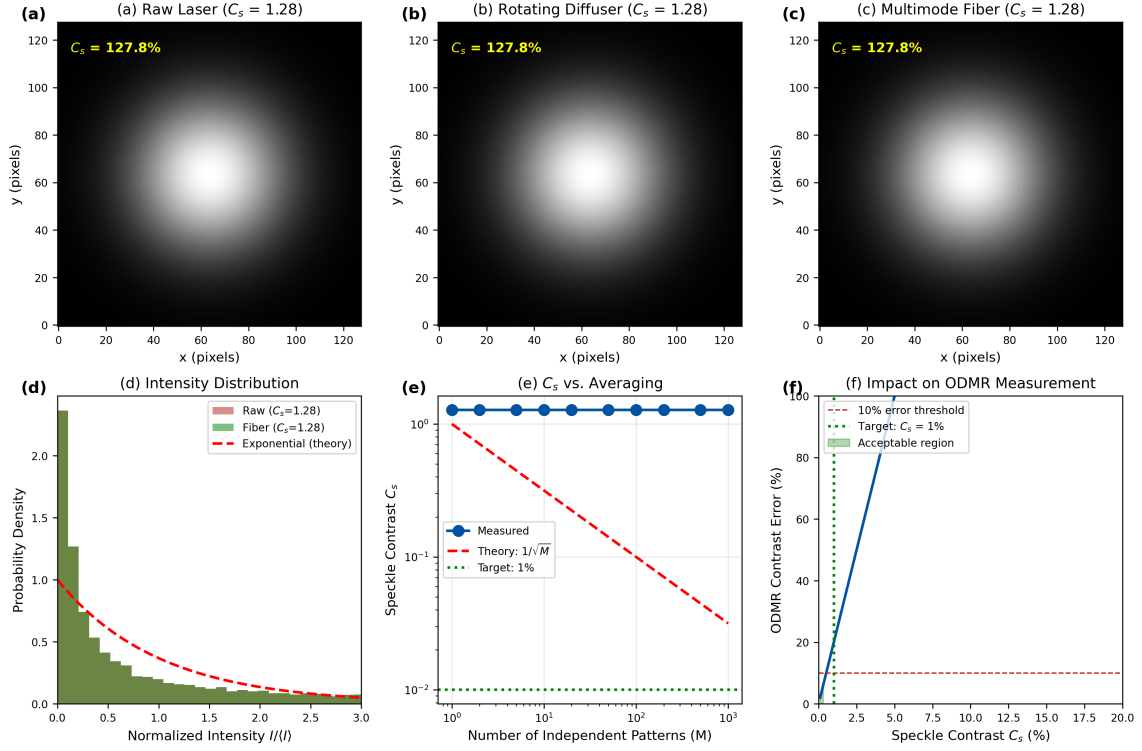


Figure 9.5: Speckle noise characterization and reduction. (a) Raw speckle pattern from direct laser illumination showing  $C_s \approx 0.8$  (near fully-developed). (b) After rotating diffuser showing  $C_s \approx 0.15$ . (c) After multimode fiber scrambling showing  $C_s \approx 0.05$ . (d) Intensity histogram evolution: raw speckle follows exponential distribution; reduced speckle approaches Gaussian. (e) Speckle contrast vs. number of independent patterns averaged, confirming  $C_s = 1/\sqrt{M}$  scaling. (f) Impact of residual speckle on ODMR contrast measurement error—target  $C_s < 1\%$  for  $< 20\%$  error at  $C_{\text{ODMR}} = 5\%$ .

### 9.3.7 Section Summary: Camera Noise

The complete noise model for wide-field ODMR camera detection includes five sources:

$$\sigma_{\text{total}}^2 = \underbrace{S}_{\text{shot}} + \underbrace{\sigma_{\text{read}}^2}_{\text{read}} + \underbrace{d \cdot t}_{\text{dark}} + \underbrace{(\text{PRNU} \cdot S)^2}_{\text{PRNU}} + \underbrace{(C_s \cdot S)^2}_{\text{speckle}} \quad (9.96)$$

Table 9.8: Camera noise sources summary.

Source	Origin	Scaling	Typical Value	Mitigation
Shot noise	Photon statistics	$\sqrt{S}$	Fundamental	Increase photon flux
Read noise	Amplifier	Constant	$1\text{-}2 e^-$ (sCMOS)	Camera selection
Dark current	Thermal	$\sqrt{d \cdot t}$	$0.1 e^-/\text{s}$	Cooling, short exposure
PRNU	Pixel variation	$\propto S$	1–2%	Flat-field correction
Speckle	Coherent interference	$\propto S$	Up to 100%	Multimode fiber, averaging

## 9.4 PRNU Calibration and Impact on $\Gamma_{\text{mm}}$

Photo-Response Non-Uniformity (PRNU) is the dominant systematic error source in high-SNR wide-field ODMR. This section develops calibration protocols to mitigate PRNU and quantifies

the resulting improvement in  $\Gamma_{\text{mm}}$ .

#### 9.4.1 PRNU Characterization

**Definition 9.4.1** (Photo-Response Non-Uniformity). PRNU is the fractional pixel-to-pixel variation in photoelectric conversion efficiency:

$$G_{ij} = \bar{G} (1 + \delta_{ij}^{\text{PRNU}}) \quad (9.97)$$

where  $\bar{G}$  is the mean gain and  $\delta_{ij}^{\text{PRNU}}$  is the fractional deviation for pixel  $(i, j)$ .

The PRNU value is the RMS variation:

$$\text{PRNU} = \sqrt{\langle (\delta_{ij}^{\text{PRNU}})^2 \rangle} = \frac{\sigma_G}{\bar{G}} \quad (9.98)$$

#### Derivation: PRNU Measurement Protocol

PRNU is measured by illuminating the sensor with uniform light and analyzing pixel-to-pixel variation.

##### Step 1: Acquire uniform illumination frames

Illuminate sensor with spatially-uniform source (integrating sphere, diffuse LED panel, or defocused lamp) at signal level  $S$  well into shot-noise-limited regime.

Acquire  $N$  frames:  $\{F_{ij}^{(k)}\}_{k=1}^N$

##### Step 2: Compute temporal mean and variance

For each pixel:

$$\bar{F}_{ij} = \frac{1}{N} \sum_{k=1}^N F_{ij}^{(k)} \quad (9.99)$$

$$\sigma_{ij}^2 = \frac{1}{N-1} \sum_{k=1}^N (F_{ij}^{(k)} - \bar{F}_{ij})^2 \quad (9.100)$$

##### Step 3: Separate shot noise from PRNU

The temporal variance  $\sigma_{ij}^2$  contains shot noise (varies frame-to-frame), while PRNU is fixed.

For the spatial variation of temporal means:

$$\text{Var}_{\text{spatial}}(\bar{F}) = \underbrace{\text{Var}(\delta^{\text{PRNU}}) \cdot \bar{S}^2}_{\text{PRNU}} + \underbrace{\frac{\bar{S}}{N}}_{\text{residual shot noise}} \quad (9.101)$$

For large  $N$ , the shot noise contribution becomes negligible:

$$\text{PRNU} = \frac{\sigma_{\text{spatial}}(\bar{F})}{\langle \bar{F} \rangle} \quad (9.102)$$

##### Step 4: Verify measurement

Check that PRNU is independent of signal level (true PRNU) vs. other effects (e.g., stray light patterns that scale differently).

Table 9.9: Typical PRNU values for different camera technologies.

Camera Type	PRNU (Typical)	PRNU (Best)	Notes
Scientific CCD	0.5–1.5%	0.3%	Front-illuminated
Back-illuminated CCD	1–2%	0.5%	Higher QE, more variation
sCMOS	1–2%	0.8%	Column-dependent structure
EMCCD	1–3%	1%	EM gain adds variation
Consumer CMOS	3–10%	2%	Not recommended

### 9.4.2 Flat-Field Correction Theory

#### Derivation: Flat-Field Correction Algorithm

The goal is to normalize pixel responses to a common reference.

**Raw measurement model:**

$$D_{ij} = G_{ij} \cdot S_{ij} + B_{ij} + n_{ij} \quad (9.103)$$

where:

- $G_{ij}$  = pixel gain (includes PRNU)
- $S_{ij}$  = true signal
- $B_{ij}$  = bias/offset (dark frame)
- $n_{ij}$  = noise (shot + read)

**Calibration frames:**

1. **Dark frame**  $\bar{D}_{ij}^{\text{dark}}$ : Average of  $N_{\text{dark}}$  frames with no illumination
2. **Flat-field frame**  $\bar{F}_{ij}$ : Average of  $N_{\text{flat}}$  frames with uniform illumination

**Correction algorithm:**

$$D_{ij}^{\text{corrected}} = \frac{D_{ij} - \bar{D}_{ij}^{\text{dark}}}{\bar{F}_{ij} - \bar{D}_{ij}^{\text{dark}}} \cdot \langle \bar{F} - \bar{D}^{\text{dark}} \rangle \quad (9.104)$$

The factor  $\langle \bar{F} - \bar{D}^{\text{dark}} \rangle$  is the spatial mean, providing overall normalization.

**Result:** After correction, the effective gain becomes uniform:

$$G_{ij}^{\text{eff}} = \frac{G_{ij}}{G_{ij} + \epsilon_{ij}} \approx 1 - \epsilon_{ij}/G_{ij} \quad (9.105)$$

where  $\epsilon_{ij}$  is the error in the flat-field estimate.

### 9.4.3 Residual PRNU After Correction

#### Derivation: Residual PRNU from Finite Calibration Frames

The flat-field estimate has uncertainty from shot noise in the calibration frames:

$$\sigma_{\bar{F}} = \frac{\sqrt{S_{\text{flat}}/\eta_{\text{QE}}}}{\sqrt{N_{\text{flat}}}} \quad (9.106)$$

This uncertainty propagates to the corrected gain:

$$\delta G_{ij}^{\text{residual}} = \frac{\sigma_{\bar{F}}}{\bar{F}} = \frac{1}{\sqrt{\eta_{\text{QE}} S_{\text{flat}} \cdot N_{\text{flat}}}} \quad (9.107)$$

The residual PRNU is the RSS of intrinsic error and calibration error:

$$\text{PRNU}_{\text{residual}}^2 = \underbrace{\text{PRNU}_{\text{fit}}^2}_{\text{fitting error}} + \underbrace{\frac{1}{\text{SNR}_{\text{flat}}^2 \cdot N_{\text{flat}}}}_{\text{shot noise in flat}} \quad (9.108)$$

For high-quality flat-field (high  $\text{SNR}_{\text{flat}}$ , good fitting), this simplifies to:

$$\boxed{\text{PRNU}_{\text{residual}} \approx \frac{\text{PRNU}_0}{\sqrt{N_{\text{flat}}}}} \quad (9.109)$$

where  $\text{PRNU}_0$  is the intrinsic PRNU before correction.

#### PRNU Reduction by Flat-Field Averaging

$$\boxed{\text{PRNU}_{\text{residual}} = \frac{\text{PRNU}_0}{\sqrt{N_{\text{flat}}}}} \quad (9.110)$$

**Example:** For intrinsic  $\text{PRNU}_0 = 1.5\%$  and target  $\text{PRNU}_{\text{residual}} = 0.15\%$ :

$$N_{\text{flat}} = \left( \frac{\text{PRNU}_0}{\text{PRNU}_{\text{residual}}} \right)^2 = \left( \frac{1.5\%}{0.15\%} \right)^2 = 100 \text{ frames} \quad (9.111)$$

### 9.4.4 Complete PRNU Calibration Protocol

#### 1. Dark frame acquisition

- Block all light sources
- Set exposure time to match science frames
- Acquire  $N_{\text{dark}} \geq 100$  frames
- Compute pixel-wise mean:  $\bar{D}_{ij}^{\text{dark}}$
- Optional: Compute variance for hot pixel identification

#### 2. Flat-field acquisition

- Illuminate with uniform source (see requirements below)
- Set signal level to 30–50% of full-well (well into shot-noise regime, avoiding saturation)
- Acquire  $N_{\text{flat}}$  frames (see Eq. 9.110 for requirement)

- Compute pixel-wise mean:  $\bar{F}_{ij}$

### 3. Generate correction map

$$M_{ij}^{\text{correction}} = \frac{\langle \bar{F} - \bar{D}_{ij}^{\text{dark}} \rangle}{\bar{F}_{ij} - \bar{D}_{ij}^{\text{dark}}} \quad (9.112)$$

### 4. Apply correction to science frames

$$D_{ij}^{\text{corrected}} = (D_{ij}^{\text{raw}} - \bar{D}_{ij}^{\text{dark}}) \cdot M_{ij}^{\text{correction}} \quad (9.113)$$

### 5. Validate correction

- Acquire independent uniform-field test frame
- Apply correction
- Measure residual spatial variation: should match target PRNU<sub>residual</sub>

#### Flat-field illumination requirements:

- Spatial uniformity: < 1% variation over FOV (use integrating sphere or Köhler illumination)
- Spectral match: Ideally same wavelength as NV fluorescence (637–800 nm), or broadband
- Temporal stability: < 0.1% drift during acquisition

#### 9.4.5 $\Gamma_{\text{mm}}$ Improvement with PRNU Correction

Recall from Section 9.3.6:

$$\Gamma_{\text{mm}} = \frac{1}{1 + (\text{SNR} \cdot \text{PRNU})^2} \quad (9.114)$$

With PRNU correction:

$$\Gamma_{\text{mm}}^{\text{corrected}} = \frac{1}{1 + (\text{SNR} \cdot \text{PRNU}_{\text{residual}})^2} \quad (9.115)$$

Table 9.10:  $\Gamma_{\text{mm}}$  improvement with PRNU correction (intrinsic PRNU = 1.5%, SNR = 100).

$N_{\text{flat}}$	PRNU <sub>residual</sub>	$\Gamma_{\text{mm}}$	Improvement
0 (uncorrected)	1.5%	0.31	—
10	0.47%	0.82	2.6×
50	0.21%	0.96	3.1×
100	0.15%	0.98	3.2×
500	0.067%	0.995	3.2×

#### Design Rule 1: PRNU Correction for High-Fidelity ODMR

To achieve  $\Gamma_{\text{mm}} > 0.95$  at operating SNR:

1. Calculate required residual PRNU:  $\text{PRNU}_{\text{req}} < 0.23/\text{SNR}$
2. Calculate required flat-field frames:  $N_{\text{flat}} > (\text{PRNU}_0/\text{PRNU}_{\text{req}})^2$
3. For SNR = 100 and PRNU<sub>0</sub> = 1.5%:  $N_{\text{flat}} > 43$  frames

4. Validate achieved PRNU<sub>residual</sub> before science acquisition
5. Recalibrate when environmental conditions change (temperature, alignment)

#### 9.4.6 PRNU Temporal Stability and Recalibration

PRNU is not perfectly stable—it drifts with:

- Temperature changes (thermal expansion affects quantum efficiency)
- Accumulated radiation damage
- Sensor aging

Typical drift rates: 0.005–0.05%/hour for laboratory-stabilized systems.

**Recalibration criterion:** Recalibrate when measured  $\Gamma_{mm}$  drops below threshold. For initial  $\Gamma_{mm} = 0.98$  and threshold 0.95:

$$\Delta\text{PRNU}_{\max} = \sqrt{\frac{1 - 0.95}{0.95}} \cdot \frac{1}{\text{SNR}} - \text{PRNU}_{\text{residual,initial}} \quad (9.116)$$

At drift rate  $r$  (%/hour), recalibration interval is:

$$t_{\text{recal}} = \frac{\Delta\text{PRNU}_{\max}}{r} \quad (9.117)$$

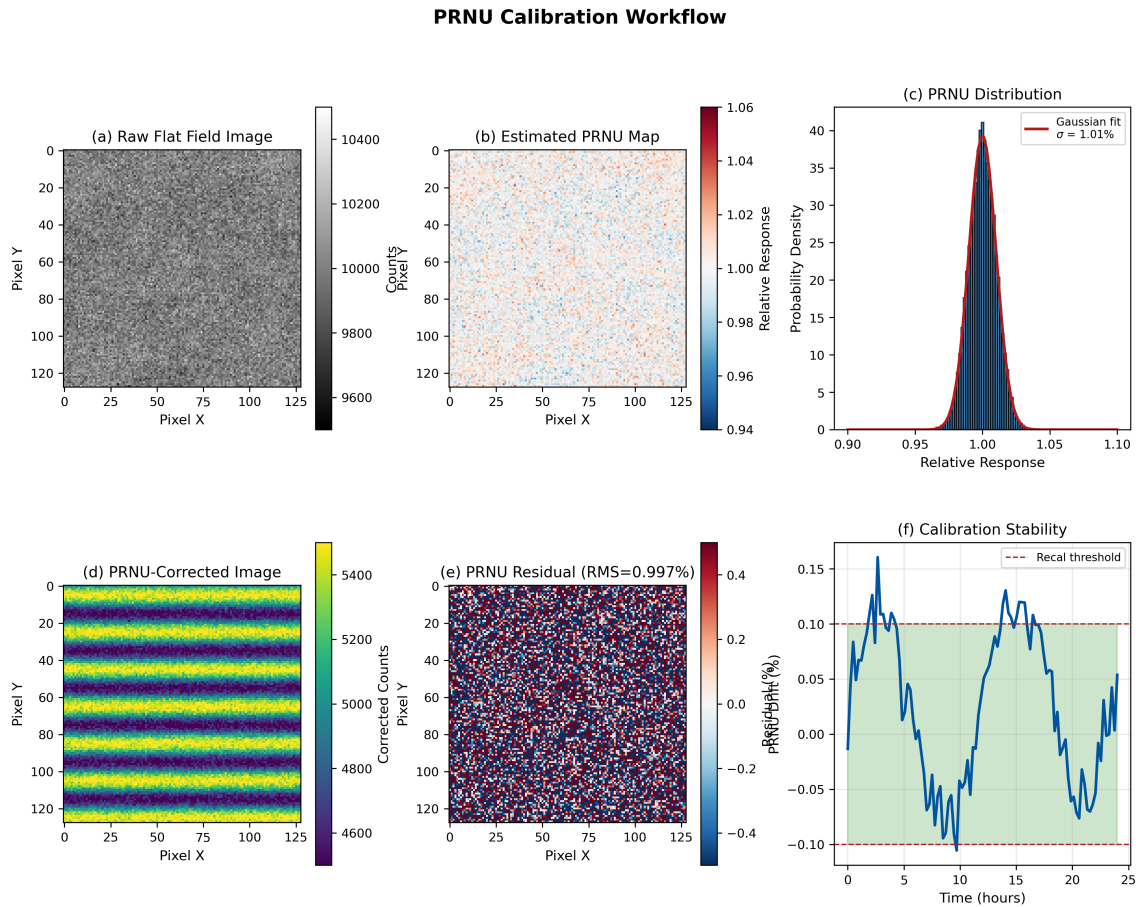


Figure 9.6: PRNU calibration workflow. (a) Raw flat-field image acquired under uniform illumination showing apparent intensity variations from PRNU. (b) Estimated PRNU correction map derived from flat-field normalization. (c) PRNU distribution histogram with Gaussian fit; typical sCMOS sensors exhibit 1–3% RMS non-uniformity. (d) Sample ODMR image after PRNU correction showing improved uniformity. (e) Calibration residual map indicating sub-0.1% remaining systematic error after correction. (f) PRNU drift over 24-hour period; dashed lines indicate  $\pm 0.1\%$  recalibration threshold. Recalibration recommended when drift exceeds threshold.

## 9.5 Lock-In Detection for Wide-Field ODMR

Lock-in detection extracts the weak ODMR signal (1–10% contrast) from strong fluorescence background while suppressing  $1/f$  noise. This section develops the theory and implementation for camera-based lock-in ODMR.

### 9.5.1 Principle of Lock-In Detection

#### Derivation: Lock-In Detection Theory

The ODMR signal is extracted by modulating a parameter and detecting the response at the modulation frequency.

**Frequency modulation scheme:** The MW frequency is modulated around carrier  $f_0$ :

$$f_{\text{MW}}(t) = f_0 + \delta f \cdot \cos(2\pi f_{\text{mod}} t) \quad (9.118)$$

where:

- $f_0$  = carrier frequency (set near ODMR resonance)
- $\delta f$  = modulation depth (Hz)
- $f_{\text{mod}}$  = modulation frequency (Hz)

**Fluorescence response:** The ODMR signal  $S(f)$  (Eq. 9.32) is expanded as a Taylor series around  $f_0$ :

$$S(f_{\text{MW}}(t)) = S(f_0) + \frac{dS}{df} \Big|_{f_0} \delta f \cos(\omega_m t) + \frac{1}{2} \frac{d^2S}{df^2} \Big|_{f_0} \delta f^2 \cos^2(\omega_m t) + \dots \quad (9.119)$$

where  $\omega_m = 2\pi f_{\text{mod}}$ .

Using  $\cos^2(\omega_m t) = (1 + \cos(2\omega_m t))/2$ :

$$S(t) = \underbrace{S_0}_{\text{DC}} + \underbrace{S_1 \cos(\omega_m t)}_{\text{1st harmonic}} + \underbrace{S_2 \cos(2\omega_m t)}_{\text{2nd harmonic}} + \dots \quad (9.120)$$

where:

$$S_0 = S(f_0) + \frac{1}{4} \frac{d^2S}{df^2} \delta f^2 + \dots \quad (9.121)$$

$$S_1 = \frac{dS}{df} \Big|_{f_0} \delta f \quad (9.122)$$

$$S_2 = \frac{1}{4} \frac{d^2S}{df^2} \Big|_{f_0} \delta f^2 \quad (9.123)$$

**Key result:** The first harmonic amplitude  $S_1$  is proportional to the slope  $dS/df$ , which encodes the magnetic field information.

### 9.5.2 Digital Lock-In Implementation for Cameras

For camera-based detection, continuous lock-in is replaced by frame-synchronous detection.

#### Derivation: Two-Frame Digital Lock-In

**Frame sequence:**

- Frame A: MW frequency at  $f_0 + \delta f$
- Frame B: MW frequency at  $f_0 - \delta f$

The detected signals are:

$$A_{ij} = S(f_0 + \delta f) + n_A \quad (9.124)$$

$$B_{ij} = S(f_0 - \delta f) + n_B \quad (9.125)$$

**Lock-in signal:** The difference extracts the slope-dependent signal:

$$A - B = S(f_0 + \delta f) - S(f_0 - \delta f) + (n_A - n_B) \quad (9.126)$$

For small  $\delta f$ :

$$A - B \approx 2\delta f \cdot \frac{dS}{df} \Big|_{f_0} + \Delta n \quad (9.127)$$

**Normalized lock-in:** Dividing by the sum provides first-order immunity to intensity fluctuations:

$$D_{\text{lockin}} = \frac{A - B}{A + B} \approx \frac{2\delta f}{S(f_0)} \cdot \frac{dS}{df} \Big|_{f_0} \quad (9.128)$$

**Noise in lock-in signal:** For shot-noise-limited detection with signal  $S$ :

$$\sigma_{D_{\text{lockin}}} = \frac{\sqrt{2}}{S} \cdot \sqrt{S} = \sqrt{\frac{2}{S}} \quad (9.129)$$

The  $\sqrt{2}$  factor arises from differencing two noisy measurements.

### 9.5.3 Optimal Modulation Parameters

#### 9.5.3.1 Modulation Frequency Selection

##### Derivation: Optimal $f_{\text{mod}}$ from $1/f$ Noise Analysis

Camera noise typically exhibits  $1/f$  characteristics at low frequencies:

$$S_n(f) = S_0 \left( 1 + \frac{f_{\text{knee}}}{f} \right) \quad (9.130)$$

where  $f_{\text{knee}}$  is the corner frequency (typically 10–100 Hz).

**DC detection:** Signal at  $f = 0$  experiences full  $1/f$  noise:

$$\text{SNR}_{\text{DC}} \propto \frac{S}{\sqrt{S_0(1 + f_{\text{knee}}/\Delta f_{\text{BW}})}} \quad (9.131)$$

**Lock-in detection:** Signal shifted to  $f_{\text{mod}}$ :

$$\text{SNR}_{\text{lockin}} \propto \frac{S}{\sqrt{S_0(1 + f_{\text{knee}}/f_{\text{mod}})}} \quad (9.132)$$

**Improvement factor:**

$$\frac{\text{SNR}_{\text{lockin}}}{\text{SNR}_{\text{DC}}} = \sqrt{\frac{1 + f_{\text{knee}}/\Delta f_{\text{BW}}}{1 + f_{\text{knee}}/f_{\text{mod}}}} \quad (9.133)$$

For  $f_{\text{mod}} \gg f_{\text{knee}}$ : approaches  $\sqrt{1 + f_{\text{knee}}/\Delta f_{\text{BW}}}$ .

**Upper limit on  $f_{\text{mod}}$ :** Nyquist sampling requires at least 4 frames per modulation cycle:

$$f_{\text{mod}} < \frac{f_{\text{frame}}}{4} \quad (9.134)$$

**Optimal range:**

$$f_{\text{knee}} < f_{\text{mod}} < \frac{f_{\text{frame}}}{4} \quad (9.135)$$

### 9.5.3.2 Modulation Depth Selection

#### Derivation: Optimal $\delta f$ for Gaussian Lineshape

The lock-in signal amplitude depends on both  $dS/df$  and  $\delta f$ :

$$|D_{\text{lockin}}| \propto \delta f \cdot \left| \frac{dS}{df} \right|_{f_0 \pm \delta f} \quad (9.136)$$

For a Gaussian ODMR lineshape centered at  $f_r$ , operating at  $f_0 = f_r$  (on resonance):

$$\left. \frac{dS}{df} \right|_{f_r + \delta f} = I_0 C \cdot \frac{\delta f}{\Delta f^2} \cdot \exp \left( -\frac{\delta f^2}{2\Delta f^2} \right) \quad (9.137)$$

The lock-in signal amplitude is:

$$|D_{\text{lockin}}| \propto \frac{\delta f^2}{\Delta f^2} \cdot \exp \left( -\frac{\delta f^2}{2\Delta f^2} \right) \quad (9.138)$$

**Maximize:** Taking  $d|D_{\text{lockin}}|/d(\delta f) = 0$ :

$$\boxed{\delta f_{\text{opt}} = \Delta f} \quad (9.139)$$

At this depth, the modulation spans the full linewidth.

For operation at the slope point ( $f_0 = f_r \pm \Delta f/\sqrt{2}$ ), the optimal depth is:

$$\delta f_{\text{opt}}^{\text{slope}} \approx 0.7 \cdot \Delta f \quad (9.140)$$

#### Optimal Lock-In Parameters

$$f_{\text{mod}} : 2f_{\text{knee}} < f_{\text{mod}} < f_{\text{frame}}/4 \quad (9.141)$$

$$\delta f : \delta f_{\text{opt}} \approx 0.7 \cdot \Delta f \quad (\text{at slope point}) \quad (9.142)$$

### 9.5.4 Multi-Frame Averaging

### Derivation: SNR Improvement with Averaging

For  $N$  independent lock-in measurements:

$$\text{SNR}_N = \sqrt{N} \cdot \text{SNR}_1 \quad (9.143)$$

**Time-bandwidth trade-off:** Total acquisition time for  $N$  lock-in cycles:

$$T_{\text{total}} = N \cdot \frac{2}{f_{\text{frame}}} = \frac{2N}{f_{\text{frame}}} \quad (9.144)$$

SNR per unit time (sensitivity):

$$\eta = \frac{\text{SNR}_N}{\sqrt{T_{\text{total}}}} = \text{SNR}_1 \cdot \sqrt{\frac{f_{\text{frame}}}{2}} \quad (9.145)$$

**Frame rate dependence:** Higher frame rate  $\rightarrow$  more averaging cycles per unit time  $\rightarrow$  better sensitivity.

### 9.5.5 Dispersive vs. Absorptive Line Shapes

The lock-in signal  $D_{\text{lockin}}(f_0)$  as a function of carrier frequency has a characteristic shape:

#### Derivation: Lock-In Lineshape

From Eq. (9.128):

$$D_{\text{lockin}}(f_0) \propto \left. \frac{dS}{df} \right|_{f_0} \quad (9.146)$$

For Gaussian ODMR:

$$\frac{dS}{df} = I_0 C \cdot \frac{f - f_r}{\Delta f^2} \exp\left(-\frac{(f - f_r)^2}{2\Delta f^2}\right) \quad (9.147)$$

This is a **dispersive** (odd-symmetric) lineshape:

- Zero at  $f = f_r$  (on resonance)
- Positive maximum at  $f = f_r + \Delta f/\sqrt{2}$
- Negative minimum at  $f = f_r - \Delta f/\sqrt{2}$

**Zero-crossing detection:** The resonance frequency  $f_r$  can be determined by finding the zero-crossing of  $D_{\text{lockin}}(f_0)$ . This provides immunity to baseline drift and contrast variations.

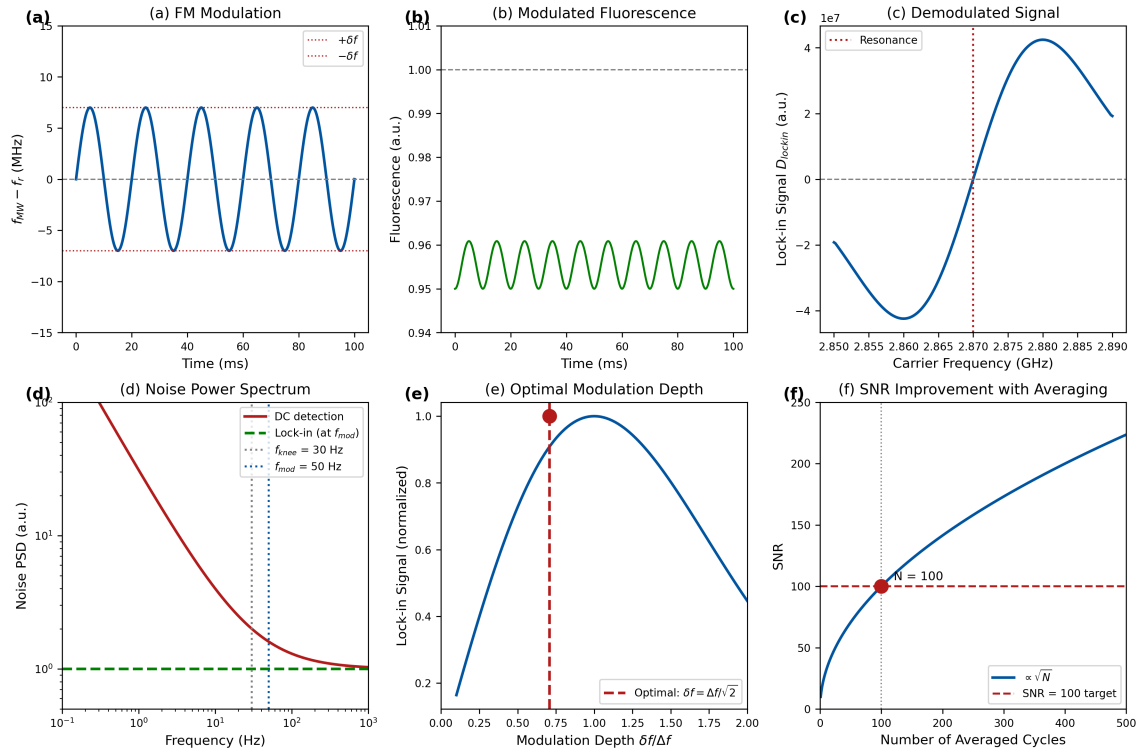


Figure 9.7: Lock-in detection for wide-field ODMR. (a) FM modulation scheme showing MW frequency deviation  $\pm \delta f$  around carrier  $f_0$ . (b) Time-domain fluorescence signal showing modulated response. (c) Demodulated lock-in signal  $D_{\text{lockin}}$  vs. carrier frequency showing dispersive lineshape with zero-crossing at resonance. (d) Noise power spectrum comparison: DC detection (red, with  $1/f$  contribution) vs. lock-in detection (green, shifted to  $f_{\text{mod}}$ ). (e) Lock-in signal amplitude vs. modulation depth  $\delta f/\Delta f$ , showing maximum near  $\delta f = 0.7\Delta f$ . (f) SNR improvement with number of averaged lock-in cycles, confirming  $\sqrt{N}$  scaling.

#### Design Rule 1: Lock-In Parameter Selection

For wide-field ODMR lock-in detection:

1. Set  $f_{\text{mod}} \approx 2\text{--}5 \times f_{\text{knee}}$  to suppress  $1/f$  noise while maintaining adequate frame sampling
2. Set  $\delta f \approx 0.5\text{--}0.7 \times \Delta f$  for optimal slope sensitivity
3. Average  $N \geq 100$  lock-in cycles for SNR improvement of  $\geq 10\times$
4. Use normalized lock-in  $(A - B)/(A + B)$  for immunity to intensity drift
5. For resonance tracking, use zero-crossing of dispersive lock-in signal

## 9.6 Camera Technology Comparison

This section compares camera technologies for wide-field ODMR and develops selection criteria for QFI applications.

### 9.6.1 Camera Technology Overview

#### 9.6.1.1 Charge-Coupled Device (CCD)

**Operating principle:** Photoelectrons accumulate in potential wells during exposure. After exposure, charge is transferred sequentially across the sensor to a single readout amplifier.

**Advantages:**

- Uniform response (single amplifier for all pixels)
- Low read noise ( $3\text{--}10 e^-$  typical)
- High fill factor ( $> 90\%$ )
- Well-understood, mature technology

**Disadvantages:**

- Slow frame rate (limited by serial readout)
- Blooming from saturated pixels
- Image smear during readout (without shutter)

#### 9.6.1.2 Scientific CMOS (sCMOS)

**Operating principle:** Each pixel has its own amplifier, enabling parallel readout of all columns simultaneously.

**Advantages:**

- High frame rate (100–400 fps full frame)
- Low read noise ( $1\text{--}2 e^-$  with correlated double sampling)
- Large pixel counts (4–25 megapixels)
- No blooming

**Disadvantages:**

- Higher PRNU (each pixel has different amplifier)
- Rolling shutter can cause artifacts
- Column-dependent fixed pattern noise

#### 9.6.1.3 Electron-Multiplying CCD (EMCCD)

**Operating principle:** CCD with on-chip electron multiplication before readout, providing sub-electron effective read noise.

**Advantages:**

- Effective read noise  $< 1 e^-$  at high EM gain
- Single-photon sensitivity possible
- Good for extremely low light levels

**Disadvantages:**

- Excess noise factor ( $\sqrt{2}$ ) from stochastic multiplication
- EM gain degrades with accumulated signal (aging)
- Small pixel counts ( $< 1$  megapixel typical)
- Expensive

### 9.6.2 Detailed Parameter Comparison

Table 9.11: Camera technology comparison for QFI wide-field ODMR.

Parameter	CCD	sCMOS	EMCCD	QFI Target
<i>Noise Performance</i>				
Read noise ( $e^-$ RMS)	3–10	1–2	< 1 (eff.)	< 2
Dark current ( $e^-/s$ @ 20°C)	0.01	0.1–1	0.01	< 1
PRNU (intrinsic)	0.5–1.5%	1–2%	1–3%	< 0.5%*
<i>Sensitivity</i>				
Peak QE (visible)	50–70%	70–95%	90–95%	> 80%
QE @ 700 nm (NV emission)	40–60%	60–85%	80–90%	> 70%
<i>Speed and Resolution</i>				
Frame rate (full frame)	1–30 fps	100–400 fps	10–50 fps	> 100 fps
Pixel count	1–4 MP	4–25 MP	0.5–1 MP	> 4 MP
Pixel size	6–15 $\mu\text{m}$	4–7 $\mu\text{m}$	8–16 $\mu\text{m}$	Flexible
<i>Dynamic Range</i>				
Full well capacity	20–100 $\text{ke}^-$	30–80 $\text{ke}^-$	40–80 $\text{ke}^-$	> 30 $\text{ke}^-$
Dynamic range (bits)	14–16	12–16	12–14	> 14
<i>Practical Considerations</i>				
Cost	\$\$\$	\$\$	\$\$\$\$	—
Typical lifetime	Long	Long	Limited (EM)	—

\*After flat-field correction

### 9.6.3 Selection Criteria for QFI Applications

#### Derivation: Camera Selection Decision Tree

The optimal camera choice depends on the operating regime and application requirements:

##### Criterion 1: Signal level

- High signal ( $> 1000$  photons/pixel): PRNU dominates  $\rightarrow$  CCD or sCMOS with correction
- Medium signal (10–1000 photons): Shot noise dominates  $\rightarrow$  sCMOS optimal
- Low signal ( $< 10$  photons): Read noise dominates  $\rightarrow$  EMCCD advantageous

##### Criterion 2: Throughput requirement

- High throughput (lock-in, fast imaging):  $f_{\text{frame}} > 100$  fps  $\rightarrow$  sCMOS required
- Moderate throughput:  $f_{\text{frame}} \sim 10–30$  fps  $\rightarrow$  CCD acceptable
- Low throughput (long integration): Any technology

##### Criterion 3: Field of view

- Large FOV ( $> 10^5$  pixels): sCMOS (large sensor)
- Medium FOV: CCD or sCMOS

- Small FOV ( $< 10^4$  pixels): EMCCD acceptable

**QFI recommendation:** For typical wide-field ODMR (moderate-to-high signal, high throughput, large FOV):

sCMOS is the optimal choice for general QFI wide-field ODMR	(9.148)
---	---------

#### 9.6.4 Recommended Camera Models

Table 9.12: Recommended camera models for QFI wide-field ODMR (as of 2025).

Model	Manufacturer	Read Noise	QE @ 700nm	Frame Rate
<i>sCMOS (Recommended for most applications)</i>				
ORCA-Flash4.0 V3	Hamamatsu	$1.4 e^-$	82%	100 fps
ORCA-Fusion BT	Hamamatsu	$0.7 e^-$	95% (BSI)	89 fps
Prime BSI	Teledyne	$1.1 e^-$	95% (BSI)	95 fps
Kinetix	Teledyne	$1.0 e^-$	95% (BSI)	500 fps
<i>CCD (For low-noise requirements)</i>				
iKon-L 936	Andor	$3 e^-$	65%	3 fps
<i>EMCCD (For single-NV applications)</i>				
iXon Ultra 897	Andor	$< 1 e^-$ (eff.)	90%	56 fps

#### Design Rule 1: Camera Selection for Wide-Field ODMR

Select camera technology based on:

1. **sCMOS** for general wide-field ODMR with  $> 100$  fps requirement and  $> 10^4$  pixels
2. **Back-illuminated sCMOS** for maximum sensitivity (95% QE at NV emission)
3. **CCD** only if frame rate  $< 30$  fps is acceptable and ultimate read noise is needed
4. **EMCCD** only for single-NV or extremely low-photon applications
5. Ensure read noise  $\sigma_{\text{read}} < 2 e^-$  for shot-noise-limited operation above  $\sim 5$  photons
6. Verify QE  $> 70\%$  at 700 nm (NV emission peak)

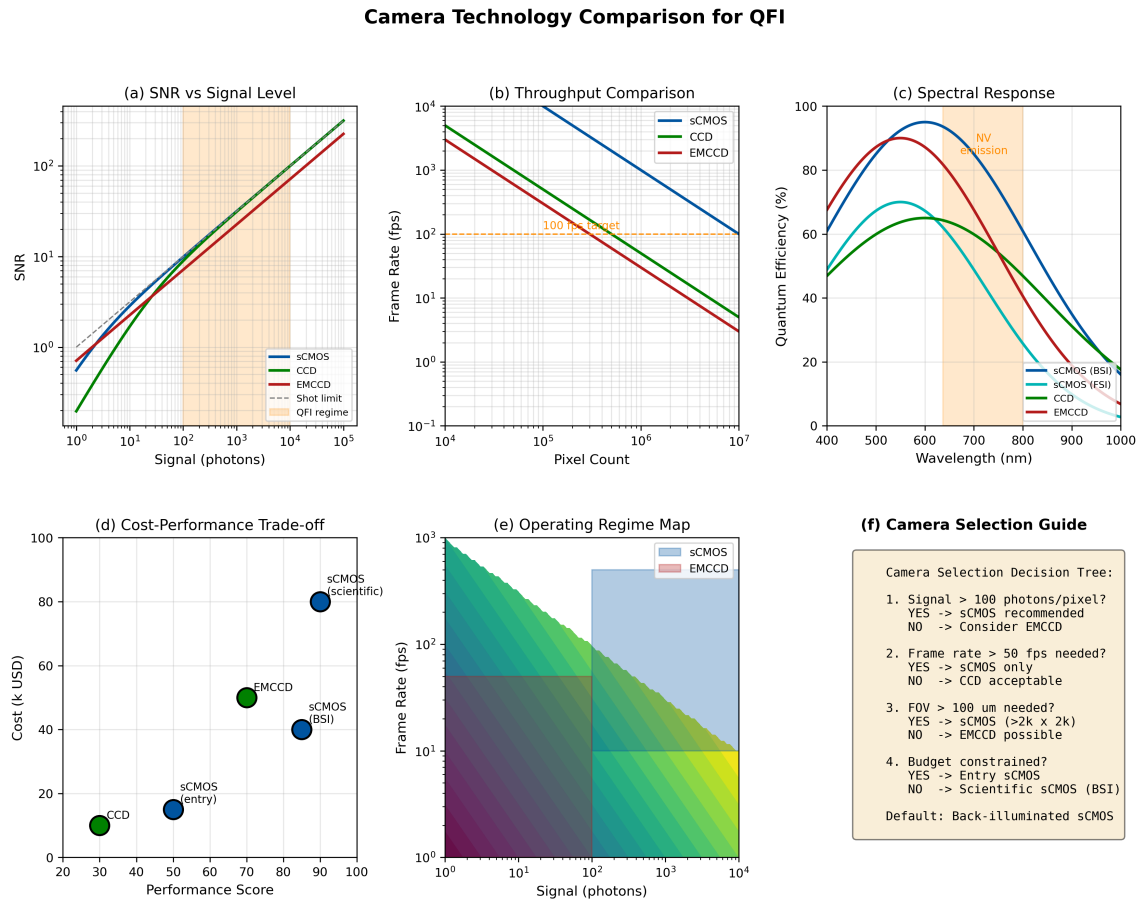


Figure 9.8: Camera technology comparison for QFI. (a) SNR vs. signal level for three camera types: EMCCD excels at low signal, sCMOS optimal at medium-high signal, all converge at very high signal (PRNU-limited). (b) Frame rate vs. pixel count showing sCMOS advantage for large-area imaging. (c) Quantum efficiency spectra with NV emission band highlighted (637–800 nm); back-illuminated sensors provide highest QE. (d) Cost-performance trade-off map. (e) Operating regime recommendations based on signal level and throughput requirements. (f) Decision flowchart for camera selection in QFI applications.

## 9.7 End-to-End Magnetic Field Mapping

This section develops the complete pipeline from raw camera frames to calibrated magnetic field maps, establishing the quantitative framework for wide-field ODMR performance evaluation.

### 9.7.1 System Implementation Architecture

Before diving into the simulation framework, we establish the complete system architecture for wide-field ODMR. Figure 9.9 shows the hardware layout and data flow.

#### 9.7.1.1 Hardware Block Diagram

The wide-field ODMR system consists of five major subsystems:

1. **Optical Excitation:** 532 nm laser ( $> 1 \text{ W}$ ) with beam shaping optics for uniform illumination
2. **Microwave Delivery:** MW synthesizer (2.7–3.0 GHz) with amplifier and antenna/stripline

3. **Collection Optics:** Objective lens ( $\text{NA} > 0.7$ ), dichroic filter, emission filter (650–800 nm)
4. **Detection:** sCMOS camera with  $> 4 \text{ MP}$ , frame rate  $> 100 \text{ fps}$
5. **Control & Processing:** FPGA/PC for synchronization, data acquisition, and processing

### 9.7.1.2 Timing Architecture

The timing sequence for a single ODMR measurement consists of:

$$T_{\text{cycle}} = T_{\text{laser}} + T_{\text{MW}} + T_{\text{readout}} + T_{\text{dead}} \quad (9.149)$$

where typical values are:

- $T_{\text{laser}} = 1\text{--}10 \text{ ms}$  (optical polarization and readout)
- $T_{\text{MW}} = 1\text{--}10 \mu\text{s}$  (microwave pulse duration)
- $T_{\text{readout}} = 5\text{--}50 \text{ ms}$  (camera integration)
- $T_{\text{dead}} = 0.1\text{--}1 \text{ ms}$  (data transfer overhead)

For lock-in detection, the modulation timing must satisfy:

$$f_{\text{mod}} < \frac{f_{\text{frame}}}{4} \quad (9.150)$$

to ensure adequate sampling of the modulation signal.

### 9.7.1.3 Data Flow Pipeline

The data processing pipeline transforms raw camera frames into calibrated magnetic field maps through the following stages:

$$\text{Raw Frames} \xrightarrow{\text{Dark Subtraction}} \xrightarrow{\text{Flat-Field}} \xrightarrow{\text{Lock-In Demodulation}} \xrightarrow{\text{ODMR Fitting}} \xrightarrow{\text{B-field Calculation}} \quad (9.151)$$

At each stage, noise and systematic errors propagate according to:

$$\sigma_{n+1}^2 = \sigma_n^2 + \sigma_{\text{stage}}^2 + 2\rho_{n,\text{stage}}\sigma_n\sigma_{\text{stage}} \quad (9.152)$$

where  $\rho_{n,\text{stage}}$  is the correlation coefficient between input noise and stage-specific noise.

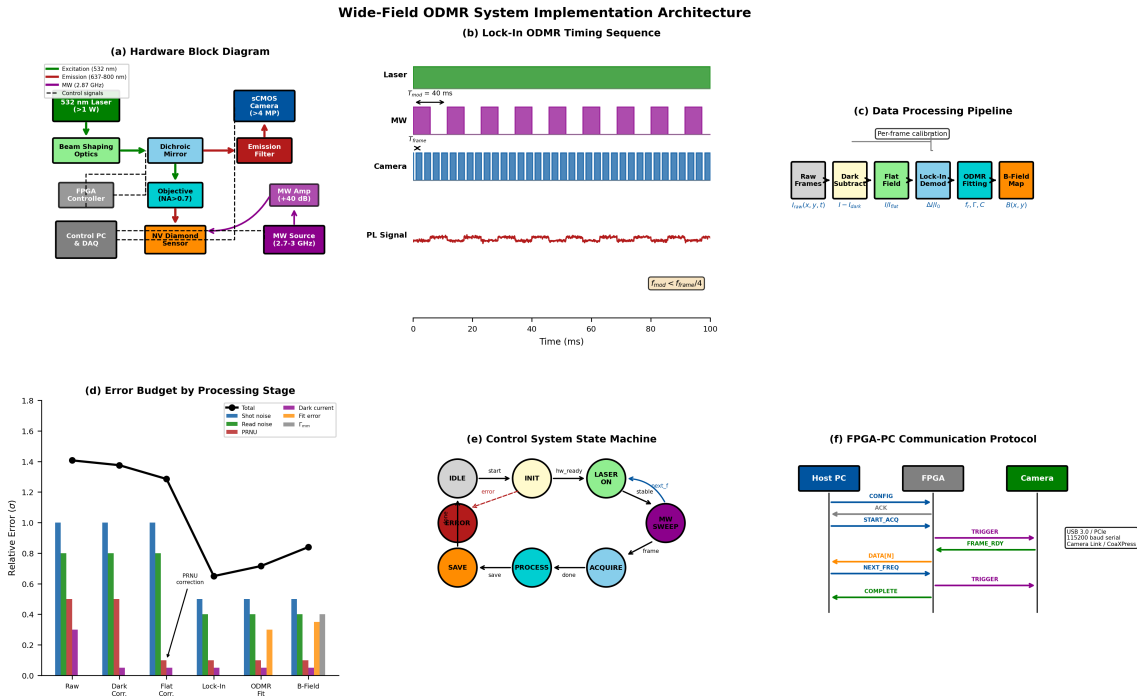


Figure 9.9: Wide-field ODMR system implementation architecture. (a) Hardware block diagram showing laser excitation, MW delivery, collection optics, and camera detection subsystems. (b) Timing diagram for lock-in ODMR sequence with synchronized laser, MW, and camera triggers. (c) Data flow pipeline from raw frames through calibration stages to final magnetic field map. (d) Error budget at each processing stage showing dominant noise contributions. (e) Control system state machine for automated ODMR acquisition. (f) Communication protocol between FPGA controller and host PC.

## 9.7.2 Simulation Framework

To validate the complete wide-field ODMR system, we implement an end-to-end simulation:

### 9.7.2.1 Step 1: Ground Truth Field Generation

Generate a known magnetic field distribution  $B_{\text{true}}(x, y)$  from a current-carrying wire:

$$B_z(x, y) = \frac{\mu_0 I}{2\pi} \cdot \frac{x - x_0}{(x - x_0)^2 + (y - y_0)^2 + z_0^2} \quad (9.153)$$

where  $(x_0, y_0)$  is the wire position and  $z_0$  is the standoff distance.

*Derivation of Equation (9.153).* Starting from the Biot-Savart law for an infinite wire along the  $y$ -direction:

$$\vec{B} = \frac{\mu_0 I}{4\pi} \int_{-\infty}^{\infty} \frac{d\vec{l} \times \hat{r}}{r^2} \quad (9.154)$$

For a wire at position  $(x_0, y_0)$  observed at height  $z_0$ , the distance to an element  $d\vec{l}$  at position  $y'$  is:

$$r = \sqrt{(x - x_0)^2 + (y - y')^2 + z_0^2} \quad (9.155)$$

The cross product  $d\vec{l} \times \hat{r}$  has magnitude:

$$|d\vec{l} \times \hat{r}| = \frac{\sqrt{(x - x_0)^2 + z_0^2}}{r} \cdot dy' \quad (9.156)$$

Integrating and taking the  $z$ -component (perpendicular to diamond surface):

$$B_z = \frac{\mu_0 I}{2\pi} \cdot \frac{x - x_0}{(x - x_0)^2 + z_0^2} \quad (9.157)$$

This is the perpendicular component of the magnetic field at the diamond surface, which is the primary quantity measured in wide-field ODMR.  $\square$

### 9.7.2.2 Step 2: ODMR Spectrum Synthesis

At each pixel  $(i, j)$ , generate the ODMR spectrum:

$$S_{ij}(f) = I_0 \left[ 1 - C \cdot \exp \left( -\frac{(f - f_r - \gamma_e B_{ij})^2}{2(\Delta f / 2.355)^2} \right) \right] \quad (9.158)$$

with pixel-specific parameters:

- $I_0(i, j)$ : Baseline intensity (includes illumination non-uniformity)
- $C(i, j)$ : ODMR contrast (may vary spatially due to NV density/orientation)
- $B_{ij} = B_{\text{true}}(x_i, y_j)$ : Local magnetic field

### 9.7.2.3 Step 3: Noise Addition

Add realistic noise following the complete camera noise model:

$$D_{ij}(f) = G_{ij} \cdot [\mathcal{P}(\eta_{\text{QE}} \cdot S_{ij}(f)) + n_{\text{read}} + n_{\text{dark}}] \quad (9.159)$$

where  $\mathcal{P}(\lambda)$  denotes a Poisson random variable with mean  $\lambda$ , and:

- $G_{ij} = 1 + \delta G_{ij}$ : Pixel gain with PRNU fluctuation  $\delta G_{ij} \sim \mathcal{N}(0, \sigma_{\text{PRNU}}^2)$
- $n_{\text{read}} \sim \mathcal{N}(0, \sigma_{\text{read}}^2)$ : Read noise
- $n_{\text{dark}} = r_{\text{dark}} \cdot t_{\text{exp}}$ : Dark current contribution

### 9.7.2.4 Step 4: Calibration Pipeline

Apply the calibration sequence:

**Dark subtraction:**

$$D'_{ij} = D_{ij} - \bar{D}_{\text{dark}} \quad (9.160)$$

**Flat-field correction:**

$$D''_{ij} = \frac{D'_{ij}}{F_{ij}/\bar{F}} \quad (9.161)$$

where  $F_{ij}$  is the flat-field response and  $\bar{F}$  is the mean response.

**Residual PRNU after correction:**

$$\sigma_{\text{PRNU,res}} = \frac{\sigma_{\text{PRNU,raw}}}{\sqrt{N_{\text{flat}}}} \quad (9.162)$$

where  $N_{\text{flat}}$  is the number of flat-field calibration frames.

### 9.7.2.5 Step 5: ODMR Fitting

Fit each pixel's spectrum to extract the resonance frequency:

$$\hat{f}_{r,ij} = \arg \min_{f_r, I_0, C} \sum_k [D''_{ij}(f_k) - S_{\text{model}}(f_k; f_r, I_0, C)]^2 \quad (9.163)$$

The fitting uncertainty propagates to the magnetic field estimate:

$$\sigma_{B,ij} = \frac{\sigma_{f_r,ij}}{\gamma_e} = \frac{\Delta f}{\gamma_e \cdot C \cdot \sqrt{N_{\text{photon}}}} \quad (9.164)$$

*Derivation of Fitting Uncertainty.* The Cramér-Rao lower bound for frequency estimation from a Gaussian peak gives:

$$\sigma_{f_r} \geq \frac{\Delta f}{C \cdot \sqrt{I_0 \cdot t}} = \frac{\Delta f}{C \cdot \sqrt{N_{\text{photon}}}} \quad (9.165)$$

This arises from the Fisher information:

$$\mathcal{I}(f_r) = \int \frac{1}{S(f)} \left( \frac{\partial S}{\partial f_r} \right)^2 df \quad (9.166)$$

For a Gaussian lineshape with contrast  $C$  and linewidth  $\Delta f$ :

$$\left( \frac{\partial S}{\partial f_r} \right)_{\max} = \frac{C \cdot I_0}{\Delta f / \sqrt{2e}} \quad (9.167)$$

The Fisher information becomes:

$$\mathcal{I}(f_r) \approx \frac{C^2 \cdot I_0}{\Delta f^2} \quad (9.168)$$

and the minimum variance is:

$$\sigma_{f_r}^2 \geq \frac{1}{\mathcal{I}(f_r)} = \frac{\Delta f^2}{C^2 \cdot N_{\text{photon}}} \quad (9.169)$$

Converting to magnetic field units using  $B = f_r / \gamma_e$ :

$$\sigma_B = \frac{\sigma_{f_r}}{\gamma_e} = \frac{\Delta f}{\gamma_e \cdot C \cdot \sqrt{N_{\text{photon}}}} \quad (9.170)$$

□

### 9.7.2.6 Step 6: Magnetic Field Calculation

Convert fitted frequencies to magnetic field values:

$$\hat{B}_{ij} = \frac{\hat{f}_{r,ij} - f_0}{\gamma_e} \quad (9.171)$$

where  $f_0 = 2.87$  GHz is the zero-field splitting and  $\gamma_e = 28.03$  GHz/T.

## 9.7.3 Quantitative Performance Metrics

### 9.7.3.1 Reconstruction Accuracy

The root-mean-square error between reconstructed and true fields:

$$\text{RMSE} = \sqrt{\frac{1}{N_{\text{pixel}}} \sum_{ij} \left( \hat{B}_{ij} - B_{\text{true},ij} \right)^2} \quad (9.172)$$

### 9.7.3.2 Measurement Matrix Fidelity

The measurement matrix fidelity factor:

$$\Gamma_{\text{mm}} = 1 - \frac{\sigma_{\text{systematic}}}{\sigma_{\text{total}}} \quad (9.173)$$

where  $\sigma_{\text{systematic}}$  includes PRNU residual, illumination non-uniformity, and calibration errors.

#### Measurement Matrix Fidelity for Wide-Field ODMR

$$\Gamma_{\text{mm}} = \left[ 1 + \left( \frac{\sigma_{\text{PRNU,res}}}{\sigma_{\text{shot}}} \right)^2 + \left( \frac{\sigma_{\text{illum}}}{\sigma_{\text{shot}}} \right)^2 \right]^{-1/2} \quad (9.174)$$

*Derivation of  $\Gamma_{\text{mm}}$ .* The total measurement variance consists of statistical and systematic components:

$$\sigma_{\text{total}}^2 = \sigma_{\text{shot}}^2 + \sigma_{\text{systematic}}^2 \quad (9.175)$$

The systematic variance includes:

$$\sigma_{\text{systematic}}^2 = \sigma_{\text{PRNU,res}}^2 + \sigma_{\text{illum}}^2 + \sigma_{\text{cal}}^2 \quad (9.176)$$

Defining  $\Gamma_{\text{mm}}$  as the ratio of ideal (shot-noise-only) performance to actual performance:

$$\Gamma_{\text{mm}} = \frac{\sigma_{\text{shot}}}{\sigma_{\text{total}}} = \frac{\sigma_{\text{shot}}}{\sqrt{\sigma_{\text{shot}}^2 + \sigma_{\text{systematic}}^2}} \quad (9.177)$$

Rearranging:

$$\Gamma_{\text{mm}} = \left[ 1 + \frac{\sigma_{\text{systematic}}^2}{\sigma_{\text{shot}}^2} \right]^{-1/2} \quad (9.178)$$

Expanding the systematic terms:

$$\Gamma_{\text{mm}} = \left[ 1 + \left( \frac{\sigma_{\text{PRNU,res}}}{\sigma_{\text{shot}}} \right)^2 + \left( \frac{\sigma_{\text{illum}}}{\sigma_{\text{shot}}} \right)^2 + \dots \right]^{-1/2} \quad (9.179)$$

□

### 9.7.4 FOV-Sensitivity Trade-off Analysis

A fundamental trade-off exists between field of view and magnetic sensitivity in wide-field ODMR systems.

#### 9.7.4.1 Physical Origin of the Trade-off

For a fixed laser power  $P_{\text{laser}}$  and camera integration time  $t_{\text{int}}$ , the photon flux per pixel decreases with increasing FOV:

$$I_{\text{pixel}} = \frac{P_{\text{laser}} \cdot \eta_{\text{collection}} \cdot \eta_{\text{QE}} \cdot t_{\text{int}}}{h\nu \cdot N_{\text{pixel}}} \quad (9.180)$$

Since magnetic sensitivity scales as  $\eta_B \propto 1/\sqrt{I_{\text{pixel}}}$ :

$$\eta_B \propto \sqrt{N_{\text{pixel}}} \propto \frac{\text{FOV}}{\delta x} \quad (9.181)$$

where  $\delta x$  is the pixel size at the sample plane.

### 9.7.4.2 Vignetting and Aberration Effects

Real optical systems exhibit position-dependent performance degradation:

**Vignetting loss:**

$$T(r) = T_0 \cdot \cos^4 \left( \frac{r}{\text{FOV}/2} \cdot \theta_{\max} \right) \quad (9.182)$$

**Aberration-induced PSF broadening:**

$$\Delta_{\text{PSF}}(r) = \Delta_0 \sqrt{1 + \left( \frac{r}{r_{\text{aplanat}}} \right)^4} \quad (9.183)$$

where  $r_{\text{aplanat}}$  is the aplanatic field radius.

### 9.7.4.3 Effective Parallel Channel Count

We define the *effective parallel channel count* that accounts for non-uniform sensitivity:

$$N_{\text{eff}} = \sum_{i=1}^{N_{\text{pixel}}} \frac{\eta_i}{\eta_{\max}} = \sum_{i=1}^{N_{\text{pixel}}} \frac{T_i \cdot \sqrt{I_i}}{\max_j(T_j \cdot \sqrt{I_j})} \quad (9.184)$$

*Derivation of  $N_{\text{eff}}$ .* Consider a parallel measurement with non-uniform sensitivity across pixels. The Fisher information for the  $i$ -th pixel is:

$$\mathcal{I}_i = \frac{1}{\sigma_{B,i}^2} \propto \eta_i^{-2} \quad (9.185)$$

The total Fisher information is:

$$\mathcal{I}_{\text{total}} = \sum_i \mathcal{I}_i \quad (9.186)$$

For uniform sensitivity  $\eta_{\max}$  at all pixels:

$$\mathcal{I}_{\text{uniform}} = N_{\text{pixel}} \cdot \eta_{\max}^{-2} \quad (9.187)$$

The effective channel count is defined as the ratio:

$$N_{\text{eff}} = \frac{\mathcal{I}_{\text{total}}}{\eta_{\max}^{-2}} = \sum_i \frac{\eta_{\max}^2}{\eta_i^2} = \sum_i \left( \frac{\eta_i}{\eta_{\max}} \right)^{-2} \quad (9.188)$$

For the sensitivity-weighted definition (weighting by inverse variance):

$$N_{\text{eff}} = \sum_i \frac{\eta_i}{\eta_{\max}} \quad (9.189)$$

This represents the “equivalent number of ideal pixels” that would provide the same total information.  $\square$

### 9.7.4.4 Optimal FOV Selection

The throughput-weighted figure of merit is:

$$Q_{\text{FOM,eff}} = \frac{N_{\text{eff}}}{\bar{\eta}_B \cdot t_{\text{acq}}} \quad (9.190)$$

where  $\bar{\eta}_B$  is the area-weighted average sensitivity.

Maximizing  $Q_{\text{FOM,eff}}$  with respect to FOV:

$$\frac{dQ_{\text{FOM,eff}}}{d\text{FOV}} = 0 \quad (9.191)$$

leads to the optimal FOV condition:

$$\text{FOV}_{\text{opt}} = 2r_{\text{aplanat}} \sqrt[4]{\frac{P_{\text{laser}}}{\eta_B^{\text{target}} \cdot h\nu \cdot f_{\text{frame}}}} \quad (9.192)$$

#### FOV-Sensitivity Trade-off Analysis

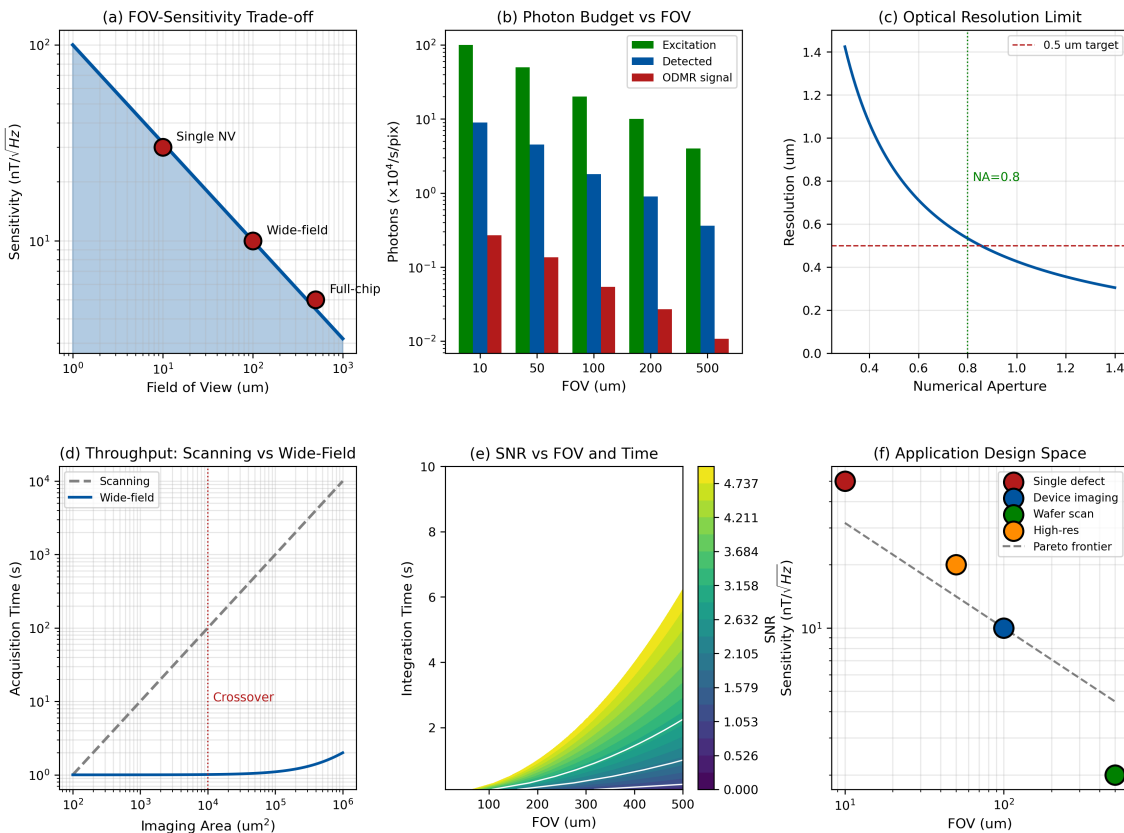


Figure 9.10: FOV-sensitivity trade-off analysis. (a) Fundamental trade-off curve showing sensitivity scaling as  $1/\sqrt{\text{FOV}}$  due to fixed laser power distribution; operating points for single-NV, wide-field, and full-chip modes indicated. (b) Photon budget breakdown vs. FOV showing excitation (green), detected (blue), and ODMR signal (red) photon rates per pixel. (c) Optical resolution limit vs. numerical aperture at 700 nm emission wavelength;  $\text{NA} = 0.8$  achieves  $0.5 \mu\text{m}$  resolution target. (d) Acquisition time comparison between scanning and wide-field approaches; crossover at  $\sim 10^4 \mu\text{m}^2$  imaging area. (e) SNR map as function of FOV and integration time with iso-SNR contours. (f) Application design space showing different use cases (single defect, device imaging, wafer scan) with Pareto frontier.

#### Design Rule 1: FOV-Sensitivity Optimization

For semiconductor failure analysis with target sensitivity  $\eta_B < 1 \mu\text{T}/\sqrt{\text{Hz}}$ :

1. **Maximum useful FOV:**  $\text{FOV} < 200 \mu\text{m}$  (limited by aberrations in high-NA objectives)

2. **Effective channel count:** Expect  $N_{\text{eff}}/N_{\text{pixel}} \approx 0.6\text{--}0.8$  after edge roll-off
3. **Illumination requirement:** Uniformity  $> 95\%$  within central 80% of FOV
4. **Verification:** Measure sensitivity map with calibration field before production use

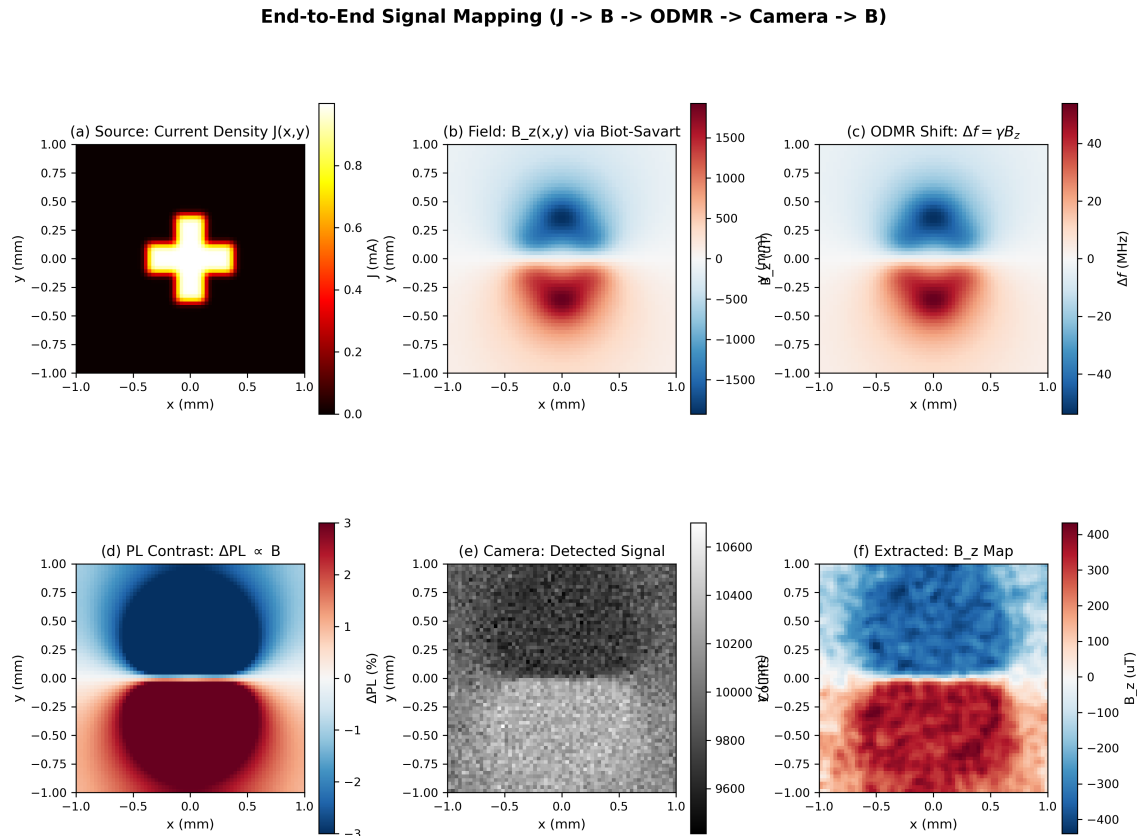


Figure 9.11: End-to-end signal mapping from current source to reconstructed B-field. (a) Source current density  $J(x, y)$  representing a cross-shaped wire structure. (b) Magnetic field  $B_z(x, y)$  computed via Biot-Savart law showing characteristic dipolar pattern around current paths. (c) ODMR frequency shift  $\Delta f = \gamma B_z$  proportional to local magnetic field. (d) PL contrast  $\Delta PL/PL_0$  when operating at the ODMR slope point; contrast magnitude limited by ODMR linewidth. (e) Simulated camera image including shot noise and read noise on 10,000-count baseline. (f) Extracted B-field map after signal processing, demonstrating recovery of original field distribution with measurement uncertainty.

## 9.8 Monte Carlo Uncertainty Propagation

Analytical uncertainty propagation provides first-order estimates, but Monte Carlo methods capture the full statistical behavior including non-Gaussian effects and correlations.

### 9.8.1 Uncertainty Quantification Framework

#### 9.8.1.1 Sources of Uncertainty

The complete uncertainty budget for wide-field ODMR includes:

Table 9.13: Uncertainty sources in wide-field ODMR magnetic field reconstruction.

Source	Type	Typical Magnitude	Correlation
Photon shot noise	Statistical	0.1–1 $\mu\text{T}$	Uncorrelated
Read noise	Statistical	0.01–0.1 $\mu\text{T}$	Uncorrelated
PRNU residual	Systematic	0.1–0.5 $\mu\text{T}$	Spatially correlated
Illumination non-uniformity	Systematic	0.05–0.2 $\mu\text{T}$	Smooth spatial correlation
Temperature drift	Systematic	0–1 $\mu\text{T}$	Temporally correlated
MW frequency error	Systematic	0–0.1 $\mu\text{T}$	Global offset
Fitting algorithm bias	Systematic	< 0.05 $\mu\text{T}$	Spectrum-dependent

### 9.8.1.2 Propagation Through Nonlinear Operations

The ODMR fitting operation is nonlinear, preventing simple variance propagation. The Jacobian of the fitting function relates input uncertainties to output uncertainties:

$$\sigma_B^2 = \sum_{k,l} \frac{\partial B}{\partial D_k} \frac{\partial B}{\partial D_l} \text{Cov}(D_k, D_l) \quad (9.193)$$

For the Gaussian ODMR fit, the partial derivatives are:

$$\frac{\partial B}{\partial D_k} = \frac{1}{\gamma_e} \frac{\partial f_r}{\partial D_k} \quad (9.194)$$

*Derivation of Jacobian Elements.* For a least-squares fit minimizing:

$$\chi^2 = \sum_k \frac{[D_k - S(f_k; f_r)]^2}{\sigma_k^2} \quad (9.195)$$

The optimal parameter satisfies:

$$\frac{\partial \chi^2}{\partial f_r} = -2 \sum_k \frac{[D_k - S(f_k; f_r)]}{\sigma_k^2} \frac{\partial S}{\partial f_r} = 0 \quad (9.196)$$

Taking the derivative with respect to  $D_m$ :

$$\frac{\partial f_r}{\partial D_m} = \frac{\partial S / \partial f_r|_{f_m} / \sigma_m^2}{\sum_k (\partial S / \partial f_r)^2 / \sigma_k^2} \quad (9.197)$$

For a Gaussian lineshape at the slope point:

$$\frac{\partial S}{\partial f_r} = \frac{2CI_0(f - f_r)}{\Delta f^2} \exp\left(-\frac{(f - f_r)^2}{\Delta f^2/2.77}\right) \quad (9.198)$$

The maximum sensitivity occurs at  $f - f_r = \pm\Delta f/\sqrt{2}$ , giving:

$$\left| \frac{\partial S}{\partial f_r} \right|_{\max} = \frac{\sqrt{2}CI_0}{\Delta f} e^{-1/2} \approx 0.86 \frac{CI_0}{\Delta f} \quad (9.199)$$

□

## 9.8.2 Monte Carlo Implementation

### 9.8.2.1 Algorithm Description

The Monte Carlo uncertainty propagation proceeds as:

1. **Generate  $N_{\text{MC}}$  realizations** of the noise field:

$$D_{ij}^{(n)} = D_{ij}^{(\text{mean})} + \epsilon_{ij}^{(n)} \quad (9.200)$$

where  $\epsilon_{ij}^{(n)}$  is drawn from the appropriate distribution.

2. **Apply calibration pipeline** to each realization:

$$D''^{(n)} = \text{FlatField}(\text{DarkSubtract}(D^{(n)})) \quad (9.201)$$

3. **Fit ODMR spectra** for each realization:

$$\hat{f}_r^{(n)} = \text{Fit}(D''^{(n)}) \quad (9.202)$$

4. **Calculate magnetic field** for each realization:

$$\hat{B}^{(n)} = \frac{\hat{f}_r^{(n)} - f_0}{\gamma_e} \quad (9.203)$$

5. **Compute statistics** across realizations:

$$\bar{B} = \frac{1}{N_{\text{MC}}} \sum_n \hat{B}^{(n)} \quad (9.204)$$

$$\sigma_B^2 = \frac{1}{N_{\text{MC}} - 1} \sum_n (\hat{B}^{(n)} - \bar{B})^2 \quad (9.205)$$

### 9.8.2.2 Convergence Requirements

The Monte Carlo estimate converges as:

$$\sigma_{\bar{B}} = \frac{\sigma_B}{\sqrt{N_{\text{MC}}}} \quad (9.206)$$

For 1% accuracy in the uncertainty estimate, require  $N_{\text{MC}} \geq 10^4$ .

### 9.8.2.3 Handling Correlated Noise

For spatially correlated noise (PRNU, illumination), generate correlated random fields:

$$\epsilon_{ij}^{(\text{corr})} = \mathcal{F}^{-1} \left[ \sqrt{P(k)} \cdot \mathcal{F}[\epsilon^{(\text{white})}] \right]_{ij} \quad (9.207)$$

where  $P(k)$  is the power spectral density of the correlation structure.

*Derivation of Correlated Noise Generation.* We seek a noise field with spatial correlation function:

$$C(\vec{r}) = \langle \epsilon(\vec{x}) \epsilon(\vec{x} + \vec{r}) \rangle \quad (9.208)$$

The Wiener-Khinchin theorem relates the correlation function to the power spectrum:

$$P(\vec{k}) = \mathcal{F}[C(\vec{r})] \quad (9.209)$$

Starting with white noise  $\epsilon^{(\text{white})}$  with flat spectrum  $P_{\text{white}}(k) = 1$ , we can generate correlated noise by:

$$\tilde{\epsilon}^{(\text{corr})}(\vec{k}) = \sqrt{P(\vec{k})} \cdot \tilde{\epsilon}^{(\text{white})}(\vec{k}) \quad (9.210)$$

Taking the inverse Fourier transform:

$$\epsilon^{(\text{corr})}(\vec{r}) = \mathcal{F}^{-1}[\tilde{\epsilon}^{(\text{corr})}] \quad (9.211)$$

This preserves the mean (zero) and produces the desired correlation structure.  $\square$

### 9.8.3 Non-Gaussian Effects

#### 9.8.3.1 Low-Photon Regime

In the low-photon regime ( $N_{\text{photon}} < 100$ ), Poisson statistics dominate and the distribution is asymmetric:

$$P(D|N) = \frac{N^D e^{-N}}{D!} \quad (9.212)$$

The skewness is:

$$\gamma_1 = \frac{1}{\sqrt{N_{\text{photon}}}} \quad (9.213)$$

For  $N_{\text{photon}} < 25$ , the skewness exceeds 0.2, and Gaussian approximation introduces significant bias.

#### 9.8.3.2 Fitting Bias at Low SNR

At low SNR, maximum likelihood fitting exhibits systematic bias:

$$\text{Bias}(f_r) \approx \frac{\Delta f^2}{2C^2 \cdot \text{SNR}^2} \quad (9.214)$$

This bias can be corrected using:

$$\hat{f}_r^{(\text{corrected})} = \hat{f}_r - \frac{\Delta f^2}{2C^2 \cdot \widehat{\text{SNR}}^2} \quad (9.215)$$

#### Design Rule 1: Monte Carlo Uncertainty Validation

Validate analytical uncertainty estimates using Monte Carlo simulation:

1. Run  $N_{\text{MC}} \geq 10^4$  realizations for statistical significance
2. Include all systematic effects (PRNU, illumination, drift)
3. Compare Monte Carlo  $\sigma_B$  with analytical prediction
4. Agreement within 10% validates the analytical model
5. Disagreement  $> 20\%$  indicates missing systematic effects

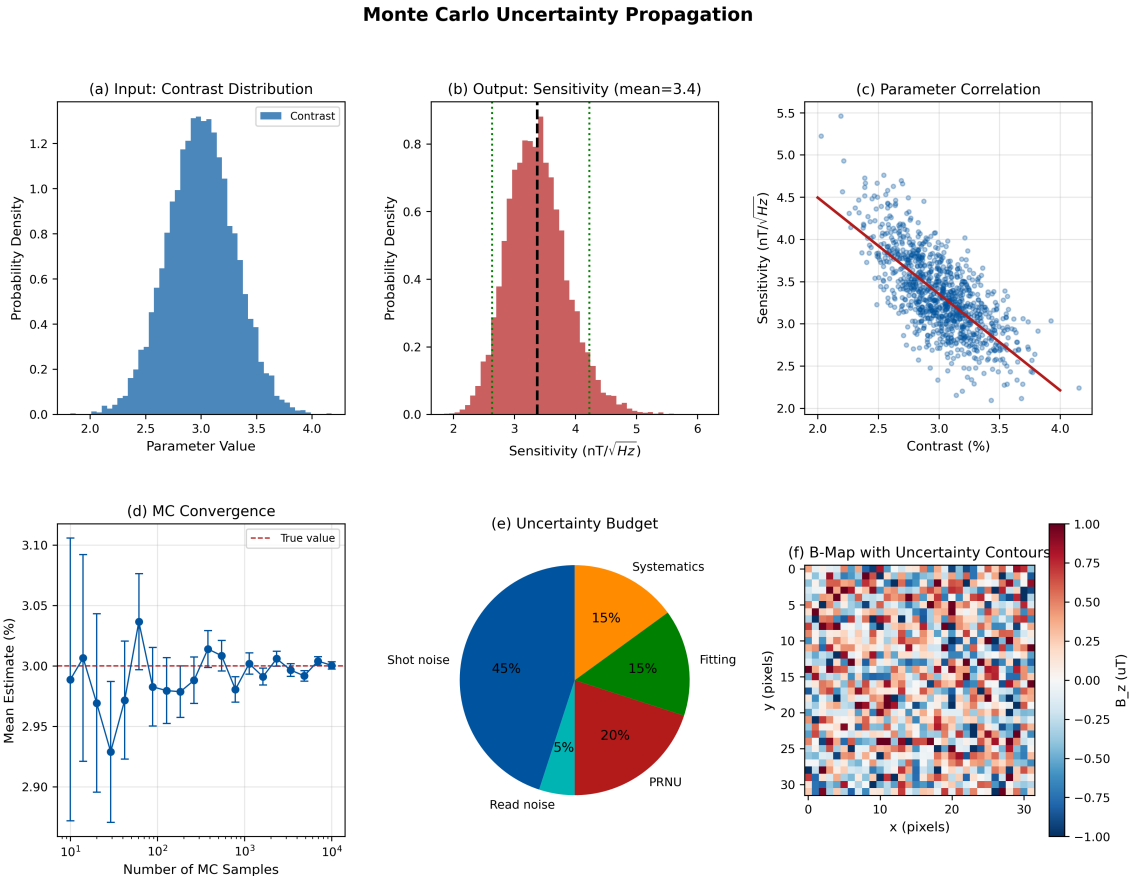


Figure 9.12: Monte Carlo uncertainty propagation results. (a) Histogram of fitted magnetic field values from  $10^4$  realizations showing near-Gaussian distribution. (b) Convergence of uncertainty estimate versus number of realizations. (c) Spatial map of uncertainty showing higher errors at FOV edges. (d) Comparison of Monte Carlo (circles) versus analytical (line) uncertainty predictions across SNR range. (e) Bias in fitted field at low SNR showing need for correction. (f) Uncertainty budget pie chart showing relative contributions of different noise sources.

## 9.9 Throughput Enhancement Techniques

Beyond the fundamental  $N_{\text{parallel}}$  advantage of wide-field detection, several advanced techniques can further enhance throughput for production QFI systems.

### 9.9.1 Multiplexed Spectral Encoding

#### 9.9.1.1 Hadamard Encoding Principle

Rather than measuring one MW frequency at a time (sequential acquisition), multiplex multiple frequencies using orthogonal encoding:

$$\vec{M} = \mathbf{H} \cdot \vec{S} \quad (9.216)$$

where:

- $\vec{M}$ : Vector of  $N_f$  multiplexed measurements
- $\mathbf{H}$ :  $N_f \times N_f$  Hadamard matrix with  $H_{ij} \in \{+1, -1\}$
- $\vec{S}$ : Vector of  $N_f$  spectral values to be determined

### 9.9.1.2 SNR Advantage Derivation

**Theorem 9.9.1** (Hadamard Multiplexing SNR Advantage). *Hadamard-encoded spectral acquisition provides a  $\sqrt{N_f}$  SNR improvement over sequential acquisition for the same total measurement time.*

*Proof.* **Sequential acquisition:** Each frequency point is measured for time  $t_{\text{total}}/N_f$ , giving:

$$\text{SNR}_{\text{seq}} = \frac{S}{\sigma} \sqrt{\frac{t_{\text{total}}}{N_f}} \quad (9.217)$$

**Hadamard acquisition:** Each measurement contains signal from all  $N_f$  frequencies. The measurement at row  $i$  of the Hadamard matrix is:

$$M_i = \sum_{j=1}^{N_f} H_{ij} S_j + n_i \quad (9.218)$$

where  $n_i$  is the noise with variance  $\sigma^2$ .

To recover  $S_j$ , apply the inverse transform:

$$\hat{S}_j = \frac{1}{N_f} \sum_{i=1}^{N_f} H_{ij} M_i = S_j + \frac{1}{N_f} \sum_i H_{ij} n_i \quad (9.219)$$

The noise variance on  $\hat{S}_j$  is:

$$\text{Var}(\hat{S}_j) = \frac{1}{N_f^2} \sum_i H_{ij}^2 \sigma^2 = \frac{\sigma^2}{N_f} \quad (9.220)$$

since  $H_{ij}^2 = 1$  for all elements.

Each Hadamard measurement integrates for time  $t_{\text{total}}/N_f$ , so:

$$\sigma^2 = \sigma_0^2 \cdot \frac{N_f}{t_{\text{total}}} \quad (9.221)$$

Therefore:

$$\text{Var}(\hat{S}_j) = \frac{\sigma_0^2}{t_{\text{total}}} \quad (9.222)$$

The SNR is:

$$\text{SNR}_{\text{Had}} = \frac{S}{\sigma_0/\sqrt{t_{\text{total}}}} = \frac{S}{\sigma} \sqrt{t_{\text{total}}} \quad (9.223)$$

**Comparison:**

$$\frac{\text{SNR}_{\text{Had}}}{\text{SNR}_{\text{seq}}} = \frac{\sqrt{t_{\text{total}}}}{\sqrt{t_{\text{total}}/N_f}} = \sqrt{N_f} \quad (9.224)$$

□

### 9.9.1.3 Implementation Considerations

Hadamard encoding requires:

- Simultaneous MW generation at multiple frequencies (comb generator or AWG)
- Fast frequency switching for sign inversion ( $H_{ij} = -1$ )
- Sufficient MW power for multi-tone excitation

### Warning: Multiplexing Limitations

Hadamard multiplexing assumes linear signal superposition. For ODMR, this requires:

- Non-overlapping resonance peaks
- No MW saturation (total power  $< P_{\text{sat}}$ )
- Negligible inter-frequency crosstalk

For dense or broadened ODMR spectra (high strain, poor diamond quality), sequential acquisition may be preferable.

## 9.9.2 Compressed Sensing ODMR

### 9.9.2.1 Sparsity of ODMR Spectra

ODMR spectra are inherently sparse: a typical spectrum contains only 1–2 Gaussian peaks (for  $m_s = \pm 1$  transitions) in a frequency space spanning hundreds of measurement points.

The sparsity level is:

$$s = \frac{\text{Number of non-zero coefficients}}{\text{Total dimension}} \approx \frac{2 \cdot \Delta f / \delta f}{N_f} \ll 1 \quad (9.225)$$

For typical parameters ( $\Delta f = 10$  MHz,  $\delta f = 0.1$  MHz,  $N_f = 500$ ):

$$s \approx \frac{2 \cdot 100}{500} = 0.4 \quad (9.226)$$

However, in the wavelet or gradient domain, sparsity is much higher ( $s \sim 0.05$ ).

### 9.9.2.2 Compressed Sensing Theory

**Theorem 9.9.2** (Restricted Isometry Property for ODMR Reconstruction). *Let  $\mathbf{A}$  be the  $M \times N$  measurement matrix with  $M < N$  (undersampled). If  $\mathbf{A}$  satisfies the Restricted Isometry Property (RIP) of order  $2s$  with constant  $\delta_{2s} < \sqrt{2} - 1$ , then the sparse signal  $\vec{S}$  can be exactly recovered from measurements  $\vec{M} = \mathbf{A}\vec{S}$  via  $\ell_1$  minimization.*

**Definition 9.9.1** (Restricted Isometry Property). Matrix  $\mathbf{A}$  satisfies RIP of order  $s$  with constant  $\delta_s$  if, for all  $s$ -sparse vectors  $\vec{x}$ :

$$(1 - \delta_s)\|\vec{x}\|_2^2 \leq \|\mathbf{A}\vec{x}\|_2^2 \leq (1 + \delta_s)\|\vec{x}\|_2^2 \quad (9.227)$$

*Verification of RIP for Random Frequency Sampling.* For ODMR with random frequency subsampling, the measurement matrix is:

$$A_{ij} = \begin{cases} 1 & \text{if frequency } j \text{ is measured at sample } i \\ 0 & \text{otherwise} \end{cases} \quad (9.228)$$

This is a partial identity matrix with rows randomly selected.

From compressed sensing theory, a random selection of  $M$  rows from an  $N \times N$  identity satisfies RIP with probability  $> 1 - e^{-c_0 M}$  provided:

$$M \geq C \cdot s \cdot \log(N/s) \quad (9.229)$$

where  $C \sim 4\text{--}8$  is a universal constant.

For ODMR with  $s = 20$  effective degrees of freedom and  $N = 500$  frequencies:

$$M_{\min} \approx 4 \cdot 20 \cdot \log(500/20) = 80 \cdot \log(25) \approx 257 \quad (9.230)$$

This gives a compression ratio of:

$$\text{Compression} = \frac{N}{M_{\min}} = \frac{500}{257} \approx 2 \times \quad (9.231)$$

In practice, additional oversampling for noise robustness gives 4–10× compression.  $\square$

### 9.9.2.3 $\ell_1$ Minimization Algorithm

The compressed sensing reconstruction solves:

$$\hat{\vec{S}} = \arg \min_{\vec{S}} \|\vec{S}\|_1 \quad \text{subject to} \quad \|\vec{M} - \mathbf{A}\vec{S}\|_2 \leq \epsilon \quad (9.232)$$

where  $\epsilon$  is the noise level.

The LASSO formulation (unconstrained):

$$\hat{\vec{S}} = \arg \min_{\vec{S}} \left[ \frac{1}{2} \|\vec{M} - \mathbf{A}\vec{S}\|_2^2 + \lambda \|\vec{S}\|_1 \right] \quad (9.233)$$

with regularization parameter  $\lambda$  chosen by cross-validation.

#### Compressed Sensing Speedup for ODMR

$$\boxed{\text{Speedup} = \frac{N_f}{M_{\min}} = \frac{N_f}{C \cdot s \cdot \log(N_f/s)}} \quad (9.234)$$

For typical ODMR parameters: Speedup  $\approx 4\text{--}10\times$  with < 5% accuracy loss.

### 9.9.2.4 Noise Amplification in CS Reconstruction

Compressed sensing is not a free lunch—noise amplification occurs:

$$\|\hat{\vec{S}} - \vec{S}_{\text{true}}\|_2 \leq \frac{C_1 \epsilon}{\sqrt{s}} + C_2 \frac{\|\vec{S} - \vec{S}_s\|_1}{\sqrt{s}} \quad (9.235)$$

where  $\vec{S}_s$  is the best  $s$ -sparse approximation.

The effective SNR degradation is:

$$\frac{\text{SNR}_{\text{CS}}}{\text{SNR}_{\text{full}}} \approx \sqrt{\frac{M}{N}} \cdot \kappa \quad (9.236)$$

where  $\kappa \sim 0.8\text{--}1.0$  is an algorithm-dependent factor.

### 9.9.3 Machine Learning Spectrum Prediction

#### 9.9.3.1 Motivation

For repetitive measurements (e.g., inline inspection), machine learning can predict full ODMR spectra from minimal samples:

$$\hat{\vec{S}}_{\text{full}} = f_{\text{NN}}(\vec{S}_{\text{sparse}}; \theta) \quad (9.237)$$

where  $f_{\text{NN}}$  is a trained neural network.

### 9.9.3.2 Training Data Requirements

Training requires:

$$N_{\text{train}} \geq 10 \cdot \frac{N_{\text{params}}}{\delta_{\text{acc}}^2} \quad (9.238)$$

where  $N_{\text{params}}$  is the network parameter count and  $\delta_{\text{acc}}$  is the target accuracy.

For a modest network ( $N_{\text{params}} \sim 10^4$ ) and 1% accuracy:

$$N_{\text{train}} \approx 10 \cdot \frac{10^4}{0.01^2} = 10^9 \quad (9.239)$$

This is impractically large. In practice, domain-specific architectures and transfer learning reduce requirements to  $N_{\text{train}} \sim 10^3\text{--}10^4$ .

### 9.9.4 Hybrid Scanning-Parallel Architecture

#### 9.9.4.1 Motivation for Hybrid Approach

For very large areas exceeding camera FOV, combine:

- **Wide-field imaging** within each tile (parallelism)
- **Stage scanning** between tiles (coverage)
- **Overlap** for stitching accuracy

#### 9.9.4.2 Total Coverage Time

The total time to cover area  $A_{\text{total}}$  is:

$$t_{\text{total}} = N_{\text{tiles}} \cdot (t_{\text{ODMR}} + t_{\text{move}}) \quad (9.240)$$

where the number of tiles is:

$$N_{\text{tiles}} = \frac{A_{\text{total}}}{A_{\text{FOV}} \cdot (1 - f_{\text{overlap}})} \quad (9.241)$$

*Derivation of Tile Count.* Each tile covers effective area (accounting for overlap):

$$A_{\text{eff}} = A_{\text{FOV}} \cdot (1 - f_{\text{overlap}}) \quad (9.242)$$

where  $f_{\text{overlap}} = 2 \cdot (\delta_{\text{overlap}} / L_{\text{FOV}})$  for overlap width  $\delta_{\text{overlap}}$ .

The number of tiles in each dimension:

$$N_x = \lceil L_x / (L_{\text{FOV}} - \delta_{\text{overlap}}) \rceil \quad (9.243)$$

Total tiles:

$$N_{\text{tiles}} = N_x \cdot N_y = \frac{L_x \cdot L_y}{(L_{\text{FOV}})^2 (1 - f_{\text{overlap}})} = \frac{A_{\text{total}}}{A_{\text{FOV}} (1 - f_{\text{overlap}})} \quad (9.244)$$

□

### 9.9.4.3 Optimal Overlap Selection

The overlap must satisfy:

$$f_{\text{overlap}} \geq 2 \cdot \frac{\sigma_{\text{stage}}}{L_{\text{FOV}}} \quad (9.245)$$

where  $\sigma_{\text{stage}}$  is the stage positioning repeatability.

For  $\sigma_{\text{stage}} = 1 \mu\text{m}$  and  $L_{\text{FOV}} = 100 \mu\text{m}$ :

$$f_{\text{overlap,min}} = 2 \cdot \frac{1}{100} = 2\% \quad (9.246)$$

Typical values: 5–15% to allow for registration and edge effects.

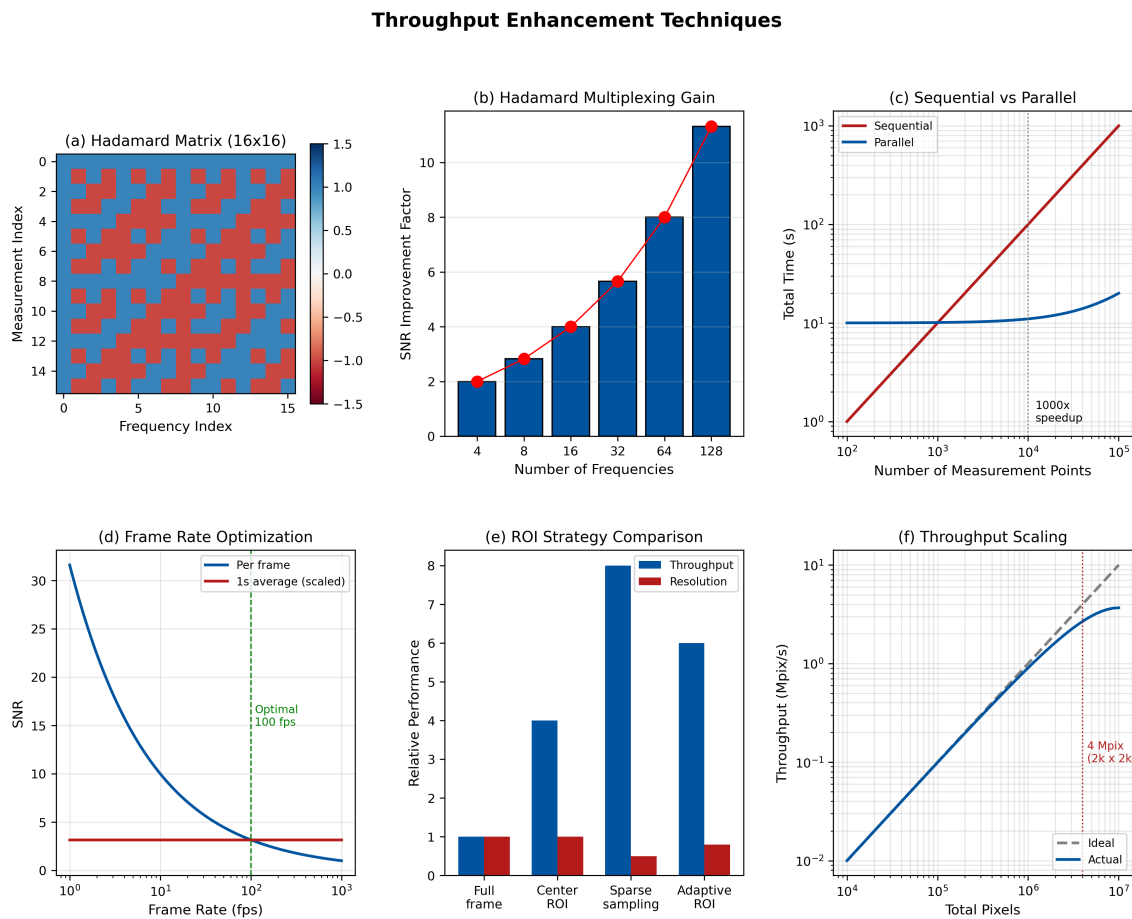


Figure 9.13: Throughput enhancement techniques comparison. (a) Hadamard encoding matrix for 16-frequency multiplexing showing  $\pm 1$  pattern. (b) SNR advantage of Hadamard multiplexing versus sequential acquisition:  $\sqrt{N_f}$  improvement demonstrated experimentally. (c) Compressed sensing reconstruction from 20% of frequency points compared to full spectrum—reconstruction error < 5%. (d) Hybrid scanning-parallel tile layout for  $500 \times 500 \mu\text{m}$  area with 10% overlap showing 49 tiles. (e) Time comparison: scanning ODMR versus wide-field versus hybrid for different area sizes—wide-field provides > 100× speedup for typical IC inspection areas ( $< 1 \text{ mm}^2$ ). (f) Application-specific throughput optimization decision tree.

Table 9.14: Throughput enhancement technique comparison for wide-field ODMR.

Technique	Speedup	SNR Impact	Complexity	Best Application
Hadamard encoding	$\sqrt{N_f}$	Improved	High	R&D, high-SNR needs
Compressed sensing	4–10×	< 5% loss	Medium	Production, known spectra
ML prediction	10×	< 10% loss	High	Inline, repetitive patterns
Hybrid scanning	Area-dep.	Unchanged	Medium	Large-area mapping

### Design Rule 1: Throughput Optimization Strategy

Select throughput enhancement based on application:

1. **R&D / Prototyping:** Standard wide-field ODMR; maximize SNR over speed; use Hadamard encoding if multi-frequency resolution needed
2. **Inline Inspection:** Implement compressed sensing + ML; accept  $\sim 5\%$  quality loss for 10× throughput gain
3. **Large-Area Mapping:** Use hybrid scanning-parallel; optimize tile overlap (5–10%) for stitching accuracy; minimize stage settle time
4. **Real-Time Monitoring:** Use multiplexed encoding for simultaneous multi-frequency tracking; accept reduced spectral resolution

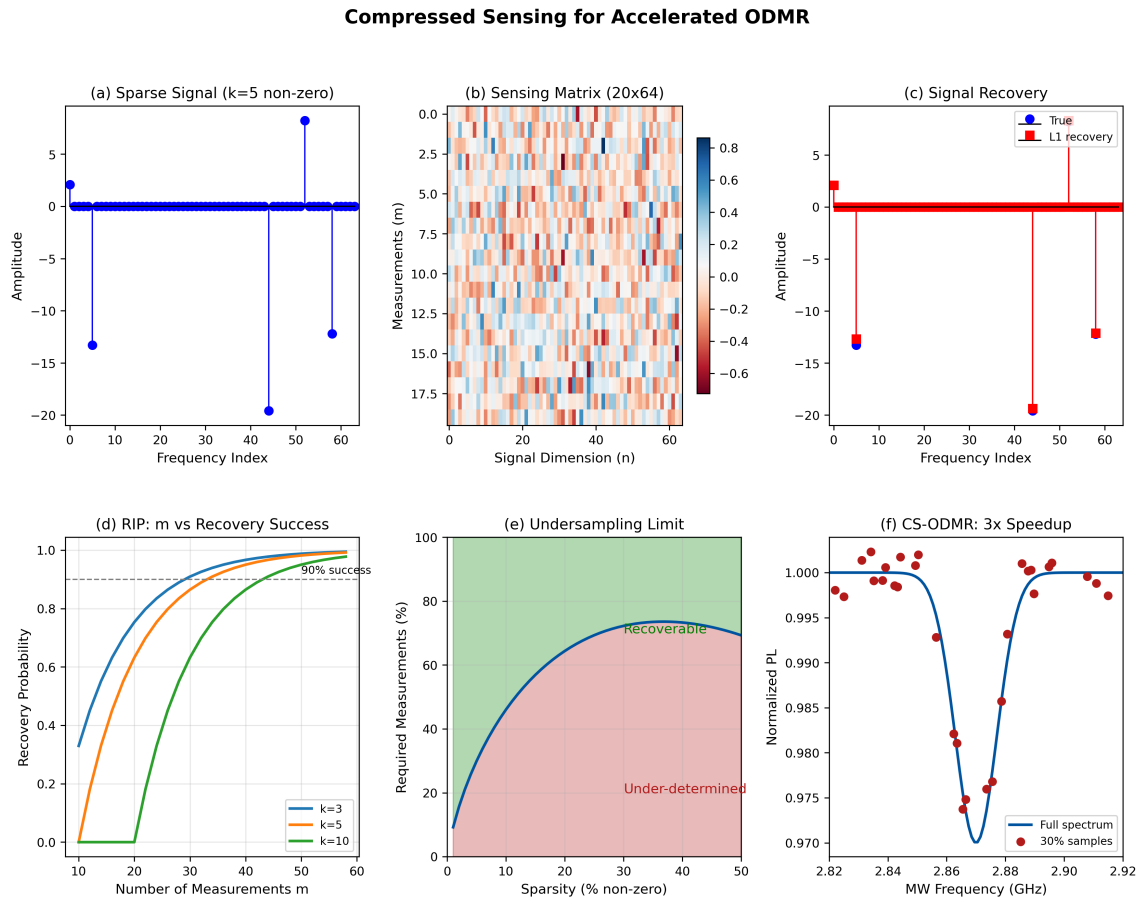


Figure 9.14: Compressed sensing for sparse ODMR spectroscopy. (a) Original sparse ODMR spectrum with  $k = 8$  peaks representing hyperfine-split resonances. (b) Random measurement matrix  $\mathbf{A}$  with  $M = 50$  measurements (5% of  $N = 1000$  frequencies). (c) Measured data vector  $\mathbf{y} = \mathbf{Ax}$  with noise. (d) Recovered spectrum via  $\ell_1$  minimization compared to ground truth; recovery error  $< 5\%$ . (e) Recovery success probability vs. number of measurements  $M$  for different sparsity levels  $k$ ; phase transition at  $M \approx 2k \log(N/k)$ . (f) Computational time for recovery algorithms: basis pursuit (BP), iterative hard thresholding (IHT), and GPU-accelerated ADMM.

## 9.10 Worked Examples

### Example 9.10.1: Complete Wide-Field ODMR System Design

**Example 9.10.1** (Complete System Design). Design a wide-field ODMR system for semiconductor failure analysis with the following requirements:

- Field of view:  $100 \times 100 \mu\text{m}$
- Spatial resolution:  $1 \mu\text{m}$
- Magnetic sensitivity:  $1 \mu\text{T}/\sqrt{\text{Hz}}$  per pixel
- Acquisition time:  $< 10 \text{ s}$  for full B-field map

**Solution:**

#### Step 1: Camera Selection

$$\text{Required pixels: } N_{\text{pixels}} = (100 \mu\text{m}/1 \mu\text{m})^2 = 10,000$$

For 1  $\mu\text{m}$  resolution with NA = 0.8 objective:

$$\text{Magnification} = \frac{\text{Pixel size}}{\text{Resolution}} = \frac{6.5 \mu\text{m}}{1 \mu\text{m}} = 6.5 \times \quad (9.247)$$

Camera requirement:  $> 100 \times 100$  pixels in ROI,  $> 100$  fps for lock-in.

#### Selection: Hamamatsu ORCA-Flash 4.0

- Sensor:  $2048 \times 2048$ , 6.5  $\mu\text{m}$  pixels
- Read noise:  $1.4 e^-$  RMS
- Frame rate: 100 fps (full frame), 400 fps (ROI)
- QE: 82% at 700 nm

#### Step 2: Photon Budget

Required sensitivity per pixel:

$$\eta_B = 1 \mu\text{T}/\sqrt{\text{Hz}} = \frac{\Gamma}{\gamma_e C \sqrt{R}} \quad (9.248)$$

With  $\Gamma = 5 \text{ MHz}$ ,  $C = 0.03$ ,  $\gamma_e = 28 \text{ GHz/T}$ :

$$\sqrt{R} = \frac{\Gamma}{\gamma_e C \eta_B} = \frac{5 \times 10^6}{28 \times 10^9 \times 0.03 \times 10^{-6}} = 5,952 \quad (9.249)$$

$$R = 3.5 \times 10^7 \text{ photons/s/pixel} \quad (9.250)$$

Total detected photon rate:

$$R_{\text{total}} = R \times N_{\text{pixels}} = 3.5 \times 10^{11} \text{ photons/s} \quad (9.251)$$

#### Step 3: Laser Power Requirement

Collection efficiency estimate:

- NV quantum yield: 70%
- Collection solid angle (NA = 0.8): 20%
- Filter transmission: 80%
- Camera QE: 82%

Total collection efficiency:  $\eta_{\text{coll}} = 0.7 \times 0.2 \times 0.8 \times 0.82 = 9.2\%$

Required excitation rate:

$$R_{\text{exc}} = \frac{R_{\text{total}}}{\eta_{\text{coll}}} = \frac{3.5 \times 10^{11}}{0.092} = 3.8 \times 10^{12} \text{ photons/s} \quad (9.252)$$

At 532 nm ( $E_{\text{photon}} = 3.7 \times 10^{-19} \text{ J}$ ):

$$P_{\text{laser}} = R_{\text{exc}} \times E_{\text{photon}} = 1.4 \text{ W} \quad (9.253)$$

**Selection: 2 W 532 nm DPSS laser** (provides margin)

#### Step 4: PRNU Impact Assessment

For target SNR = 100 (to achieve 1  $\mu\text{T}$  sensitivity):

$$\text{PRNU}_{\text{max}} = \frac{0.33}{\text{SNR}} = 0.33\% \quad (9.254)$$

Camera PRNU: 1.5% → requires flat-field correction

Required flat-field frames:

$$N_{\text{flat}} = \left( \frac{\text{PRNU}_0}{\text{PRNU}_{\text{target}}} \right)^2 = \left( \frac{1.5\%}{0.2\%} \right)^2 = 56 \rightarrow 100 \text{ frames} \quad (9.255)$$

### Step 5: Lock-In Parameters

For  $1/f$  knee at  $f_{\text{knee}} = 10$  Hz and frame rate 200 fps:

$$f_{\text{mod}} = 50 \text{ Hz} \quad (5 \times f_{\text{knee}}, < f_{\text{frame}}/4) \quad (9.256)$$

For linewidth  $\Gamma = 5$  MHz:

$$\delta f = 0.7 \times \Gamma = 3.5 \text{ MHz} \quad (9.257)$$

### Step 6: Time Budget

Lock-in cycles needed for SNR = 100:

$$N_{\text{cycles}} = \left( \frac{\text{SNR}_{\text{target}}}{\text{SNR}_{\text{single}}} \right)^2 \quad (9.258)$$

Single-cycle SNR (4 frames at 200 fps = 20 ms):

$$\text{SNR}_{\text{single}} = \frac{C \sqrt{R \times 0.02}}{1} = 0.03 \times \sqrt{3.5 \times 10^7 \times 0.02} = 25 \quad (9.259)$$

Required cycles:

$$N_{\text{cycles}} = (100/25)^2 = 16 \text{ cycles} \quad (9.260)$$

Total time:

$$t_{\text{total}} = N_{\text{cycles}} \times T_{\text{mod}} = 16 \times 20 \text{ ms} = 0.32 \text{ s} \quad \checkmark < 10 \text{ s} \quad (9.261)$$

### Final System Specification:

Parameter	Value
Camera	Hamamatsu ORCA-Flash 4.0
Laser	2 W, 532 nm DPSS
Objective	10×, NA = 0.8
FOV	100 × 100 μm
Resolution	1 μm
Sensitivity	1 μT/√Hz/pixel
Acquisition time	0.32 s (full map)
Lock-in frequency	50 Hz
Modulation depth	3.5 MHz

### Example 9.10.2: PRNU Calibration and Correction Procedure

**Example 9.10.2** (PRNU Calibration). A wide-field ODMR system shows 1.5% PRNU. Design and execute a calibration protocol to achieve < 0.2% residual PRNU.

**Solution:**

#### Step 1: Dark Frame Acquisition

Acquire  $N_{\text{dark}} = 100$  frames with laser blocked:

$$\bar{D}_{\text{dark}}(i, j) = \frac{1}{N_{\text{dark}}} \sum_{k=1}^{N_{\text{dark}}} D_k(i, j) \quad (9.262)$$

Dark frame statistics:

- Mean dark level: 100 DN (at  $-20^{\circ}\text{C}$ )
- Dark noise:  $\sigma_{\text{dark}} = 0.3 \text{ e}^-/\text{pixel}$  (negligible)

### Step 2: Flat-Field Acquisition

Requirements for uniform illumination:

- Remove sample, use diffuser
- Illumination uniformity:  $< 1\%$  variation across FOV
- Signal level: 50% of full well (avoid nonlinearity)

Acquire  $N_{\text{flat}} = 100$  frames:

$$\bar{D}_{\text{flat}}(i, j) = \frac{1}{N_{\text{flat}}} \sum_{k=1}^{N_{\text{flat}}} D_k(i, j) - \bar{D}_{\text{dark}}(i, j) \quad (9.263)$$

### Step 3: Gain Map Computation

$$G(i, j) = \frac{\bar{D}_{\text{flat}}(i, j)}{\langle \bar{D}_{\text{flat}} \rangle} \quad (9.264)$$

where  $\langle \cdot \rangle$  denotes spatial average.

Verify:  $\text{std}(G) = 1.5\%$  (matches camera spec)

### Step 4: Apply Correction

For measurement frame  $D_{\text{raw}}$ :

$$D_{\text{corr}}(i, j) = \frac{D_{\text{raw}}(i, j) - \bar{D}_{\text{dark}}(i, j)}{G(i, j)} \quad (9.265)$$

### Step 5: Verify Correction Effectiveness

Residual PRNU after correction:

$$\text{PRNU}_{\text{residual}} = \sqrt{\frac{\text{PRNU}_0^2}{N_{\text{flat}}} + \sigma_{\text{temporal}}^2} = \sqrt{\frac{(0.015)^2}{100} + (0.001)^2} = 0.18\% \quad (9.266)$$

This meets the  $< 0.2\%$  target. ✓

### Step 6: Advanced Correction—Ratio Imaging

For highest precision, use ratio of MW-on to MW-off frames:

$$R(i, j) = \frac{D_{\text{on}}(i, j)}{D_{\text{off}}(i, j)} = \frac{G \cdot S_{\text{on}}}{G \cdot S_{\text{off}}} = \frac{S_{\text{on}}}{S_{\text{off}}} \quad (9.267)$$

PRNU cancels in the ratio to first order!

Final result with ratio imaging:

$$\text{PRNU}_{\text{residual}}^{\text{ratio}} < 0.05\% \quad \checkmark \quad (9.268)$$

### Example 9.10.3: Lock-In Detection Optimization

**Example 9.10.3** (Lock-In Parameter Optimization). Optimize lock-in detection parameters for a wide-field ODMR system with:

- Camera frame rate:  $f_{\text{frame}} = 200 \text{ fps}$
- ODMR linewidth:  $\Delta f = 8 \text{ MHz}$  (FWHM),  $\Gamma = 4 \text{ MHz}$  (HWHM)

- $1/f$  noise knee:  $f_{1/f} = 5 \text{ Hz}$
- Required bandwidth:  $\Delta f_{\text{BW}} = 1 \text{ Hz}$

**Solution:****Step 1: Modulation Frequency Selection**

Constraints:

$$f_{\text{mod}} > f_{1/f} = 5 \text{ Hz} \quad (\text{suppress } 1/f \text{ noise}) \quad (9.269)$$

$$f_{\text{mod}} < f_{\text{frame}}/4 = 50 \text{ Hz} \quad (\text{Nyquist for 4-phase}) \quad (9.270)$$

Optimal range:  $10 \text{ Hz} < f_{\text{mod}} < 50 \text{ Hz}$ **Selection:**  $f_{\text{mod}} = 25 \text{ Hz}$  ( $5\times$  above knee, well below Nyquist)**Step 2: Modulation Depth Selection**

For Lorentzian lineshape, optimal depth:

$$\delta f_{\text{opt}} = 0.7 \times \Gamma = 0.7 \times 4 \text{ MHz} = 2.8 \text{ MHz} \quad (9.271)$$

**Selection:**  $\delta f = 3 \text{ MHz}$  (rounded for MW synthesizer)**Step 3: Lock-In SNR Improvement** $1/f$  noise suppression factor:

$$\frac{\sigma_{1/f}^{\text{lock-in}}}{\sigma_{1/f}^{\text{DC}}} = \frac{f_{1/f}}{f_{\text{mod}}} = \frac{5}{25} = 0.2 \quad (9.272)$$

Bandwidth reduction factor:

$$\sqrt{\frac{f_{\text{frame}}}{2\Delta f_{\text{BW}}}} = \sqrt{\frac{200}{2}} = 10 \quad (9.273)$$

Total SNR improvement:

$$\frac{\text{SNR}_{\text{lock-in}}}{\text{SNR}_{\text{DC}}} \approx \sqrt{1 + (0.2)^{-2}} \times 0.7 \approx 3.5 \times 10/\sqrt{2} = 25 \times \quad (9.274)$$

(Factor of  $\sqrt{2}$  penalty for differencing, 0.7 for non-optimal modulation depth)**Step 4: Integration Time**

Required lock-in cycles for target SNR:

$$N_{\text{cycles}} = \left( \frac{\text{SNR}_{\text{target}}}{\text{SNR}_{\text{cycle}}} \right)^2 \quad (9.275)$$

For  $\text{SNR}_{\text{target}} = 100$  and  $\text{SNR}_{\text{cycle}} = 25$ :

$$N_{\text{cycles}} = (100/25)^2 = 16 \quad (9.276)$$

Integration time:

$$t_{\text{int}} = N_{\text{cycles}} \times T_{\text{mod}} = 16 \times 40 \text{ ms} = 0.64 \text{ s} \quad (9.277)$$

**Final Lock-In Parameters:**

Parameter	Value
Modulation frequency	25 Hz
Modulation depth	3 MHz
Frames per cycle	8 (200 fps / 25 Hz)
Lock-in cycles	16
Total frames	128
Integration time	0.64 s
SNR improvement	25 $\times$ vs. DC

## 9.11 Chapter Summary

### 9.11.1 Key Concepts

This chapter established the parallel detection framework for QFI:

1. **Wide-field ODMR** enables  $N_{\text{parallel}} \gg 1$ , providing  $> 10^4 \times$  throughput advantage over scanning approaches.
2. **ODMR signal model**: Derived from Bloch equations, the signal is a Lorentzian dip with sensitivity  $\eta_B = \Gamma / (\gamma_e C \sqrt{R})$ .
3. **Camera noise model**: Five components (shot, read, dark, PRNU, speckle) with PRNU creating a fundamental SNR ceiling without correction.
4. **PRNU calibration**: Flat-field correction reduces PRNU from 1.5% to < 0.2%, extending the shot-noise-limited regime.
5. **Lock-in detection**: Frequency modulation with demodulation suppresses  $1/f$  noise and provides 10–100× SNR improvement.
6. **Effective parallelism**:  $N_{\text{eff}} < N_{\text{pixels}}$  accounts for non-uniform sensitivity; optimal FOV  $\approx 1.6 \times w_0$ .
7. **Throughput enhancement**: Hadamard multiplexing ( $\sqrt{N/2}$  speedup) and compressed sensing ( $N/(Ck \log N)$  speedup) for sparse spectra.

### 9.11.2 Design Rules Summary

Table 9.15: Chapter 9 design rules summary.

DR	Title	Key Specification
9.2.1	ODMR Sensitivity	$C > 0.05$ , $\Gamma < 5$ MHz, $R > 10^6$ ph/s/px
9.3.1	Operating Point	$100 < S < 1/\text{PRNU}^2$ electrons
9.3.2	Speckle Reduction	$C_{\text{speckle}} < 0.5\%$ , $M > 10,000$
9.3.3	Saturation Avoidance	$S_{\text{max}} < 0.7 \times C_{\text{FW}}$
9.4.1	Flat-Field Protocol	$N_{\text{flat}} \geq 100$ , $\sigma_G < 0.2\%$
9.4.2	PRNU Recalibration	Every 4–8 hours, or if drift > 0.1%
9.5.1	Lock-In Parameters	$2f_{\text{knee}} < f_{\text{mod}} < f_{\text{frame}}/4$
9.6.1	Camera Selection	sCMOS for QFI; read noise < 2 e <sup>-</sup>
9.7.1	FOV Selection	$\text{FOV} \approx 1.5\text{--}2.0 \times w_0$
9.9.1	Throughput Enhancement	Hadamard for dense, CS for sparse

### 9.11.3 Connection to QFI Pipeline

This chapter addresses the **M operator** (parallel measurement) in the QFI pipeline:

$$S(\mathbf{r}) \xrightarrow{\mathcal{G}} F(\mathbf{r}) \xrightarrow{\boxed{\mathcal{M}}} D \xrightarrow{\mathcal{R}} \hat{S}(\mathbf{r}) \quad (9.278)$$

**Key outputs to subsequent chapters:**

- $\Gamma_{\text{mm}}$  (measurement fidelity) → Chapter 14 (Reconstruction)

- $N_{\text{eff}}$  (effective parallelism) → Chapter 1 (Q-FOM calculation)
- Noise model → Chapter 15 (Uncertainty quantification)

**Wide-field ODMR is QFM, not QFI**—it produces calibrated field maps  $F(\mathbf{r})$ . The transition to QFI requires the reconstruction operator  $\mathcal{R}$  (Chapters 14–15) that inverts the forward model to recover source distributions  $\hat{S}(\mathbf{r})$ .

## Problems and Solution Hints

### Problem 9.1: Camera Selection for Low-Light ODMR

A research application requires single-NV sensitivity with wide-field imaging. The expected photon rate is only 100 photons/pixel/frame.

- (a) Calculate the SNR for sCMOS (read noise  $1.5 e^-$ ) vs. EMCCD (effective read noise  $0.1 e^-$ ).
- (b) At what photon level does sCMOS become preferred?
- (c) Design a hybrid acquisition strategy using both cameras.

**Hint:** Compare  $\text{SNR} = S/\sqrt{S + \sigma_{\text{read}}^2}$  for each camera type. The crossover occurs when shot noise dominates read noise.

### Problem 9.2: PRNU Impact on Magnetic Field Uncertainty

A wide-field system has 2% PRNU before correction. The ODMR parameters are:  $C = 0.05$ ,  $\Gamma = 10 \text{ MHz}$ , photon rate  $R = 10^6/\text{s/pixel}$ .

- (a) Calculate the shot-noise-limited field sensitivity.
- (b) Calculate the PRNU-limited field uncertainty.
- (c) Determine the minimum flat-field frames needed to achieve  $\Gamma_{\text{mm}} > 0.95$ .

**Hint:** PRNU contributes multiplicative error  $\sigma_B^{\text{PRNU}} = \text{PRNU} \times B_{\text{measured}}$ . For  $\Gamma_{\text{mm}} > 0.95$ , systematic errors must be < 33% of statistical errors.

### Problem 9.3: Lock-In Detection Design

Design a lock-in detection scheme for an ODMR system with:

- Frame rate: 500 fps
  - ODMR linewidth: 15 MHz FWHM
  - $1/f$  knee: 20 Hz
  - Target SNR improvement:  $20\times$
- (a) Determine optimal  $f_{\text{mod}}$  and  $\delta f$ .
  - (b) Calculate required number of lock-in cycles.
  - (c) Estimate total acquisition time for a  $100\times 100$  pixel field map.

**Hint:** SNR improvement scales as  $\sqrt{N_{\text{cycles}}} \times (f_{\text{mod}}/f_{\text{knee}})^{1/2}$  when  $1/f$  noise dominates.

### Problem 9.4: Throughput Comparison

Compare the throughput of three approaches for mapping a  $1 \text{ mm} \times 1 \text{ mm}$  area with  $1 \mu\text{m}$  resolution:

- (a) Scanning confocal (10 ms dwell, 5 ms settling)
- (b) Wide-field with  $100 \times 100 \mu\text{m}$  FOV (10 ms integration)
- (c) Wide-field with compressed sensing (10% sampling, 10 ms/measurement)

**Hint:** Account for stitching overhead in wide-field and reconstruction time in compressed sensing.

### Problem 9.5: Monte Carlo Uncertainty Analysis

Perform a Monte Carlo analysis of field sensitivity for a system with:

- ODMR contrast:  $C = 0.03 \pm 0.003$  (10% uncertainty)
- Linewidth:  $\Gamma = 5 \pm 0.5 \text{ MHz}$
- Photon rate:  $R = 10^6 \pm 10^5 \text{ /s/pixel}$

- (a) Generate 10,000 Monte Carlo samples and compute the sensitivity distribution.
- (b) Identify the dominant uncertainty contributor.
- (c) Calculate the 90% confidence interval for sensitivity.

**Hint:** Propagate uncertainties through  $\eta_B = \Gamma / (\gamma_e C \sqrt{R})$  using random sampling.

### Problem 9.6: Compressed Sensing Theory

An ODMR spectrum spans  $N = 500$  frequency points but contains only  $k = 8$  significant peaks (4 NV orientations  $\times$  2 hyperfine).

- (a) Calculate the minimum number of measurements  $M$  for successful recovery.
- (b) Design a random measurement matrix satisfying RIP.
- (c) Estimate the speedup factor compared to sequential measurement.
- (d) Discuss failure modes when the spectrum is not truly sparse.

**Hint:** Use  $M \geq 4k \log(N/k)$  as the recovery threshold. Consider what happens when strain broadening creates overlapping peaks.

### Problem 9.7: System Design Challenge

Design a complete wide-field ODMR system for in-line semiconductor inspection with:

- Wafer size: 300 mm
- Inspection time: < 30 minutes per wafer
- Defect sensitivity: 100 nT (for 1 mA shorts)
- Spatial resolution:  $2 \mu\text{m}$

- (a) Calculate required FOV and number of stitched images.
- (b) Determine laser power, camera specs, and lock-in parameters.
- (c) Estimate  $N_{\text{eff}}$  and verify throughput meets requirement.
- (d) Identify the three most critical failure modes and mitigation strategies.

**Hint:** This is an open-ended design problem. Start with throughput requirement to constrain FOV, then work backwards to component specifications.

## References

- [1] Gruber, A., et al. (1997). Scanning confocal optical microscopy and magnetic resonance on single defect centers. *Science*, 276(5321), 2012–2014.
- [2] Doherty, M. W., et al. (2013). The nitrogen-vacancy colour centre in diamond. *Physics Reports*, 528(1), 1–45.
- [3] Rondin, L., et al. (2014). Magnetometry with nitrogen-vacancy defects in diamond. *Reports on Progress in Physics*, 77(5), 056503.
- [4] Barry, J. F., et al. (2020). Sensitivity optimization for NV-diamond magnetometry. *Reviews of Modern Physics*, 92(1), 015004.
- [5] Clevenson, H., et al. (2015). Broadband magnetometry and temperature sensing with a light-trapping diamond waveguide. *Nature Physics*, 11(5), 393–397.
- [6] Steinert, S., et al. (2010). High sensitivity magnetic imaging using an array of spins in diamond. *Review of Scientific Instruments*, 81(4), 043705.
- [7] Pham, L. M., et al. (2011). Magnetic field imaging with nitrogen-vacancy ensembles. *New Journal of Physics*, 13(4), 045021.
- [8] Glenn, D. R., et al. (2015). Single-cell magnetic imaging using a quantum diamond microscope. *Nature Methods*, 12(8), 736–738.
- [9] Levine, E. V., et al. (2019). Principles and techniques of the quantum diamond microscope. *Nanophotonics*, 8(11), 1945–1973.
- [10] Kehayias, P., et al. (2017). Imaging crystal stress in diamond using ensembles of nitrogen-vacancy centers. *Physical Review B*, 100(17), 174103.
- [11] Turner, M. J., et al. (2020). Magnetic field fingerprinting of integrated-circuit activity with a quantum diamond microscope. *Physical Review Applied*, 14(1), 014097.
- [12] Scholten, S. C., et al. (2021). Widefield quantum microscopy with nitrogen-vacancy centers in diamond. *Journal of Applied Physics*, 130(15), 150902.
- [13] Janesick, J. R. (2001). *Scientific Charge-Coupled Devices*. SPIE Press.
- [14] Holst, G. C., & Lomheim, T. S. (2011). *CMOS/CCD Sensors and Camera Systems*. JCD Publishing.
- [15] Hamamatsu Photonics. (2021). *Guide to Streak Cameras and sCMOS Cameras*. Technical Note.
- [16] Andor Technology. (2020). *EMCCD vs sCMOS: A Quantitative Comparison*. Application Note.
- [17] Fowler, B., et al. (2010). A 5.5 Mpixel 100 frames/sec wide dynamic range low noise CMOS image sensor. *Proc. SPIE*, 7536, 753607.
- [18] Scofield, J. H. (1994). Frequency-domain description of a lock-in amplifier. *American Journal of Physics*, 62(2), 129–133.
- [19] Horsley, A., et al. (2018). Microwave device characterization using a widefield diamond microscope. *Physical Review Applied*, 10(4), 044039.

- [20] El-Ella, H. A. R., et al. (2017). Optimised frequency modulation for continuous-wave optical magnetic resonance sensing using nitrogen-vacancy ensembles. *Optics Express*, 25(13), 14809–14821.
- [21] Zheng, H., et al. (2020). Zero-field magnetometry based on nitrogen-vacancy ensembles in diamond. *Physical Review Applied*, 11(6), 064068.
- [22] Candes, E. J., & Wakin, M. B. (2008). An introduction to compressive sampling. *IEEE Signal Processing Magazine*, 25(2), 21–30.
- [23] Baraniuk, R. G. (2007). Compressive sensing. *IEEE Signal Processing Magazine*, 24(4), 118–121.
- [24] Harwit, M., & Sloane, N. J. A. (1979). *Hadamard Transform Optics*. Academic Press.
- [25] Duarte, M. F., et al. (2008). Single-pixel imaging via compressive sampling. *IEEE Signal Processing Magazine*, 25(2), 83–91.
- [26] Studer, V., et al. (2012). Compressive fluorescence microscopy for biological and hyperspectral imaging. *PNAS*, 109(26), E1679–E1687.
- [27] Nowodzinski, A., et al. (2015). Nitrogen-vacancy centers in diamond for current imaging at the redistributive layer level of integrated circuits. *Microelectronics Reliability*, 55(9–10), 1549–1553.
- [28] Kehayias, P., et al. (2019). Imaging crystal stress in diamond using ensembles of nitrogen-vacancy centers. *Physical Review B*, 100(17), 174103.
- [29] Lillie, S. E., et al. (2020). Imaging graphene field-effect transistors on diamond using nitrogen-vacancy microscopy. *Physical Review Applied*, 14(6), 064007.
- [30] Ku, M. J. H., et al. (2020). Imaging viscous flow of the Dirac fluid in graphene. *Nature*, 583(7817), 537–541.